Establishing the structure of GeS_2 at high pressures and temperatures: a combined approach using x-ray and neutron diffraction

2009 J. Phys.: Condens. Matter 21 474217

(http://iopscience.iop.org/0953-8984/21/47/474217)

J. Phys.: Condens. Matter **21** (2009) 474217 (22pp) doi:10.1088/0953-8984/21/47/474217

Establishing the structure of GeS_2 at high pressures and temperatures: a combined approach using x-ray and neutron diffraction

Anita Zeidler[1], James W E Drewitt[1], Philip S Salmon[1], Adrian C Barnes[2], Wilson A Crichton[3], Stefan Klotz[4], Henry E Fischer[5], Chris J Benmore[6], Silvia Ramos[7] and Alex C Hannon[8]

[1] Department of Physics, University of Bath, Bath BA2 7AY, UK
[2] H H Wills Physics Laboratory, Royal Fort, Tyndall Avenue, Bristol BS8 1TL, UK
[3] European Synchrotron Radiation Facility, 6 rue Jules Horowitz, BP 220, Grenoble Cedex, F-38043, France
[4] IMPMC, Université Pierre et Marie Curie F-75252 Paris, France
[5] Institut Laue-Langevin, 6 rue Jules Horowitz, BP 156, Grenoble Cedex 9, F-38042, France
[6] Argonne National Laboratory, 9700 South Cass Avenue, Argonne, IL 60439, USA
[7] Diamond Light Source Ltd, Diamond House, Harwell Science and Innovation Campus, Didcot, Oxon OX11 0DE, UK
[8] ISIS Facility, Rutherford Appleton Laboratory, Chilton, Didcot, Oxon OX11 0QX, UK

Received 17 April 2009, in final form 4 August 2009
Published 5 November 2009
Online at stacks.iop.org/JPhysCM/21/474217

Abstract

The change in structure of glassy GeS_2 with pressure increasing to $\simeq$5 GPa at ambient temperature was explored by using *in situ* neutron and x-ray diffraction. Under ambient conditions, the glass structure is made from a mixture of corner- and edge-sharing $Ge(S_{1/2})_4$ tetrahedra where 47(5)% of the Ge atoms are involved in edge-sharing configurations. The network formed by these tetrahedra orders on an intermediate range as manifested by the appearance of a pronounced first sharp diffraction peak in the measured total structure factors at a scattering vector $k = 1.02(2)$ Å^{-1} which has a large contribution from Ge–Ge correlations. The intermediate range order breaks down when the pressure on the glass increases above $\approx$2 GPa but there does not appear to be a significant alteration of the Ge–S coordination number or corresponding bond length with increasing density. The results for the glass are consistent with a densification mechanism in which there is a replacement of edge-sharing by corner-sharing Ge centred tetrahedral motifs and/or a reduction in the Ge–$\hat{S}$–Ge bond angle between corner-sharing tetrahedral motifs with increasing pressure. The change in structure with increasing temperature at a pressure of $\simeq$5 GPa was also investigated by means of *in situ* x-ray diffraction as the glass crystallized and then liquefied. At 5.2(1) GPa and 828(50) K the system forms a tetragonal crystal, with space group $I\bar{4}2d$ and cell parameters $a = b = 4.97704(12)$ and $c = 9.5355(4)$ Å, wherein corner-sharing $Ge(S_{1/2})_4$ tetrahedra pack to form a dense three-dimensional network. A method is described for correcting x-ray diffraction data taken *in situ* under high pressure, high temperature conditions for a cylindrical sample, container and gasket geometry with a parallel incident beam and with a scattered beam that is defined using an oscillating radial collimator. A method is also outlined for obtaining coordination numbers from direct integration of the peaks in measured x-ray total pair distribution functions.

(Some figures in this article are in colour only in the electronic version)

1. Introduction

Glasses with the AX_2 stoichiometry are at the heart of many materials of scientific and technological importance [1], where A denotes an electropositive species such as Si, Ge or Zn and X denotes an electronegative species such as O, S, Se or Cl. In these materials the basic structural motifs, which are usually $A(X_{1/2})_4$ tetrahedra, link to form a network in which two characteristic length scales appear at distances greater than the nearest-neighbour [2–6]. One of these length scales is associated with an intermediate range and manifests itself by the appearance of a so-called first sharp diffraction peak (FSDP) in the measured diffraction patterns at a scattering vector k_{FSDP} where $k_{\mathrm{FSDP}}r_{\mathrm{AX}} \simeq 2.5$ and r_{AX} is the nearest-neighbour distance for unlike chemical species [7–9]. The other is associated with an extended range which has a periodicity given by $\simeq 2\pi/k_{\mathrm{PP}}$ where k_{PP} denotes the scattering vector of the principal peak and $k_{\mathrm{PP}}r_{\mathrm{AX}} \simeq 4.8$ [6]. The nature of the network can be changed substantially by altering the type and connectivity of the basic structural motifs via a change in the atomic constituents or adjustment of the temperature and pressure. This leads to an interplay between the importance of the ordering on the intermediate and extended length scales [4, 6].

For example, in the case of the archetypical 'strong' glass forming system GeO_2 [10], the glass network under ambient conditions is made from an arrangement of corner-sharing $Ge(O_{1/2})_4$ tetrahedra [4, 11]. When the pressure is increased to $\approx$15 GPa, *in situ* x-ray and neutron diffraction experiments show that the FSDP changes significantly, by moving to progressively higher k-values and merging with the principal peak, as the network reorganizes to form a dense octahedral glass [12]. In comparison, $GeSe_2$ is a more 'fragile' glass forming system than GeO_2 [13] and the glass network under ambient conditions is made predominantly from a mixture of corner- and edge-sharing $Ge(Se_{1/2})_4$ tetrahedra with a small but significant number of homopolar or 'wrong' bonds [14, 15]. When the pressure on this glass is increased from ambient to 9.3 GPa, *in situ* x-ray diffraction experiments show a breakdown of the intermediate range order, as manifested by a disappearance of the FSDP, whereas the extended range order is enhanced, as manifested by a gain in intensity of the principal peak [16]. Similar behaviour is observed for the liquid phase of $GeSe_2$ as the density is increased at constant temperature by applying a pressure between 0.5 and 4.1 GPa at 1120 K [17]. When the temperature of the liquid is increased at much lower pressures, the density first increases [18] and neutron diffraction experiments show a disruption of the network as manifested by a disappearance of the FSDP [19, 20].

It is therefore of interest to understand the relation between the ordering on different length scales and the topological features of network structures. In this context, the GeS_2 system has long been regarded as an important test case for examining contrasting models for topological disorder [21], especially as the crystal structures form both two-dimensional (2D) [22] and three-dimensional (3D) [23] networks under ambient conditions. These crystal structures differ by the way in which the basic structural motifs, $Ge(S_{1/2})_4$ tetrahedra, interconnect: the former comprises chains of corner-sharing motifs linked by edge-sharing motifs to form a layered structure whereas the latter comprises a network of purely corner-sharing motifs. Pressure should be a sensitive probe of the network topology of the glass since the stronger ('intra-molecular') bonds within layer-like assemblies of motifs should be less sensitive to change in density as compared to the weaker 'inter-molecular' bonds between such assemblies [21]. More recently, these ideas have been extended to include the notion of polyamorphism i.e. the ability of a liquid or glass to undergo an abrupt change in structure with change of state variables, analogous to the polymorphic transitions that occur between different crystalline structures of the same compound [24]. The structural changes observed for liquid $GeSe_2$ under high pressure and high temperature conditions may provide evidence for such a 2D to 3D transformation [17].

In the present work a combination of x-ray and neutron diffraction is used to investigate the changes in structure that occur for glassy GeS_2 when (i) the pressure is increased to $\simeq$5 GPa at room temperature and (ii) the temperature is increased at this high pressure to induce crystallization and eventual liquefaction. Part of the motivation is provided by the structural analogies that exist between GeS_2 and $GeSe_2$ [25–29] and by the previous x-ray and neutron diffraction work on liquid and glassy $GeSe_2$ which shows that substantial structural alterations occur with change of density [30]. The information provided by these experiments does, however, focus on the topological as opposed to chemical ordering of the network. This follows from the close similarity in the atomic form factors for Ge and Se, and the close similarity in the coherent neutron scattering lengths for Ge and Se of natural isotopic abundance, which means that conventional x-ray and neutron diffraction experiments amount to a measurement of the Bhatia–Thornton [31] number–number partial structure factor $S_{\mathrm{NN}}(k)$ [20, 32, 33]. In contrast, there is a significant difference in both the x-ray form factors of Ge and S and their coherent neutron scattering lengths which means that x-ray and neutron diffraction experiments provide more information on the chemical ordering. In addition, unlike the case of $GeSe_2$, the bond lengths in GeS_2 are significantly different which aids in the interpretation of the measured pair distribution functions. Although the crystallization of amorphous GeS_2 under pressure increasing to 9 GPa has been investigated by x-ray diffraction [34], along with the structure of permanently densified GeS_2 glasses [35], little information has been obtained on the glass structure as a function of pressure and temperature by *in situ* diffraction techniques. An exception is the early x-ray diffraction work of Tanaka [36] on the glass structure at pressures up to 7 GPa made using Mo Kα radiation and a diamond anvil cell. Like $GeSe_2$, the GeS_2 system is also a more fragile glass former than GeO_2 [37, 38].

The paper is organized as follows. The essential theory required for understanding the x-ray and neutron diffraction experiments is described in section 2. The experimental method is then given in section 3 in five distinct subsections. In the first, the method used to prepare the glassy GeS_2 samples is outlined and, in the second, the neutron and x-ray diffraction experiments made under ambient temperature

and pressure conditions are reported. In the third, the x-ray diffraction experiments made *in situ* under (i) high pressure and ambient temperature or (ii) high pressure and high temperature conditions are described and, in the fourth, an account is given of the procedure required for the x-ray data reduction. In the fifth, the neutron diffraction experiments made *in situ* under high pressure and ambient temperature conditions are reported. The results are then presented in section 4 in six distinct subsections. In the first, the structure of glassy GeS_2 at ambient temperature and pressure is described. The changes in this structure observed by x-ray diffraction are then given, starting with the pressure dependence of the glass structure at room temperature. The structure of the glass recovered from high pressure is then described, followed by the structure of GeS_2 at high pressures and high temperatures, and ending with the structure of crystalline GeS_2 as measured *in situ* under high pressure and high temperature conditions. Finally, in the sixth subsection the structure of glassy GeS_2 at high pressure and ambient temperature, as determined by *in situ* neutron diffraction experiments, is described. The results are discussed in section 5 and conclusions are drawn in section 6.

2. Theory

In an x-ray or neutron diffraction experiment on glassy GeS_2 the coherent scattered intensity can be represented by the total structure factor [39]

$$F(k) = \sum_{\alpha=1}^{n}\sum_{\beta=1}^{n} c_\alpha c_\beta f_\alpha(k) f_\beta^*(k)[S_{\alpha\beta}(k) - 1] \qquad (1)$$

where α and β denote the chemical species, $n = 2$ is the number of different chemical species, c_α represents the atomic fraction of chemical species α, $f_\alpha(k)$ and $f_\alpha^*(k)$ are the scattering length (or form factor) and its complex conjugate for chemical species α, $S_{\alpha\beta}(k)$ is a Faber–Ziman [40] partial structure factor and k is the scattering vector. $S_{\alpha\beta}(k)$ is related to the partial pair distribution function $g_{\alpha\beta}(r)$ by the Fourier transform relation

$$g_{\alpha\beta}(r) - 1 = \frac{1}{2\pi^2 n_0 r}\int_0^\infty \mathrm{d}k\, k[S_{\alpha\beta}(k) - 1]\sin(kr) \qquad (2)$$

where n_0 is the atomic number density and r is a distance in real space. The scattering lengths are independent of k for the case of neutron diffraction experiments but not for the case of x-ray diffraction experiments. In order to compensate for this k dependence, the total structure factor can be re-written as

$$S(k) - 1 = \frac{F(k)}{|\langle f(k)\rangle|^2} \qquad (3)$$

where $\langle f(k)\rangle = c_\alpha f_\alpha(k) + c_\beta f_\beta(k)$ is the mean scattering length. We note that this function should be interpreted with care because the weighting factors for the $S_{\alpha\beta}(k)$ functions are k dependent. The corresponding real space information is provided by the total pair distribution function which is obtained from the Fourier transform relation

$$G(r) - 1 = \frac{1}{2\pi^2 n_0 r}\int_0^\infty \mathrm{d}k\, k[S(k) - 1]\sin(kr). \qquad (4)$$

For the case of x-ray diffraction experiments, the normalization defined by equation (3) has the advantage that it allows for a better resolution of the peaks in $G(r)$. For r values smaller than the distance of closest approach between the centre of two atoms $g_{\alpha\beta}(r) = g_{\alpha\beta}(r = 0) = 0$ such that $G(r) = G(r = 0) = 0$. The mean coordination number of atoms of type β, contained in a volume defined by two concentric spheres of radii r_i and r_j centred on an atom of type α, is given by

$$\bar{n}_\alpha^\beta = 4\pi\, n_0\, c_\beta \int_{r_i}^{r_j} \mathrm{d}r\, r^2 g_{\alpha\beta}(r). \qquad (5)$$

In practice, the measured reciprocal space functions will be subjected to a modification function $M(k)$ which results, for example, in truncation of the data sets at some maximum value $k_{\max}$ owing to the finite measurement window function of a diffractometer. In consequence, equation (4) needs to be modified and it is convenient to re-write it as

$$\begin{aligned} r[G'(r) - 1] &= \frac{1}{2\pi^2 n_0}\int_0^\infty \mathrm{d}k\, k[S(k) - 1]\, M(k)\sin(kr) \\ &= r[G(r) - 1] \otimes M(r) \end{aligned} \qquad (6)$$

where $\otimes$ denotes the one-dimensional convolution operator. In this expression the function $r[G(r) - 1]$ is convoluted with a symmetrical $M(r)$ function. For example, the measurement window is usually represented by the step function $M(k) = 1$ for $|k| \leqslant k_{\max}$, $M(k) = 0$ for $|k| > k_{\max}$ whence $M(r) = \sin(k_{\max}r)/\pi r$. Alternatively, the adoption of a Lorch [41] modification function $M(k) = \sin(ak)/(ak)$ for $|k| \leqslant k_{\max}$, $M(k) = 0$ for $|k| > k_{\max}$ gives $M(r) = [\mathrm{Si}(\pi(r + a)/a) - \mathrm{Si}(\pi(r - a)/a)]/2\pi a$ where $a = \pi/k_{\max}$ and the sine integral $\mathrm{Si}(x) \equiv \int_0^x \sin(t)/t\, \mathrm{d}t$ [5]. If the oscillations in the structure factor have not ceased before $k_{\max}$ then an application of the Lorch or related modification function will give a smoother pair correlation function at all r values by comparison with the use of a step modification function but at the expense of a loss in resolution of the first peaks in r space. We note that for r values smaller than the distance of closest approach between the centre of two atoms $G'(r) = G'(r = 0) = 0$ (see appendix A).

The notation $S_{\mathrm{X}}(k)$ and $S_{\mathrm{N}}(k)$ will be used in order to distinguish between the total structure factors measured by x-ray and neutron diffraction and the corresponding total pair distribution functions will be labelled by $G'_{\mathrm{X}}(r)$ and $G'_{\mathrm{N}}(r)$, respectively. The method used to extract coordination numbers $\bar{n}_\alpha^\beta$ from integration over peaks in $G'_{\mathrm{X}}(r)$, which is more complicated than in the case of neutron diffraction owing to the occurrence of k dependent scattering lengths, is outlined in appendix A. This integration procedure avoids the process whereby a peak shape function in r space is assumed and its Fourier transform is then fitted to the reciprocal space data at high k values. The coherent neutron scattering lengths for Ge and S are $b_{\mathrm{Ge}} = 8.185(20)$ and $b_{\mathrm{S}} = 2.847(1)$ fm [42]. The partial structure factors in $S_{\mathrm{X}}(k)$ and $S_{\mathrm{N}}(k)$ are therefore weighted differently: the ratio of the Ge to S scattering lengths $f_{\mathrm{Ge}}(k)/f_{\mathrm{S}}(k)$ is equal to 2.875 for all k values in the case of neutron diffraction but, at $k = 0$, is equal to 2 in the case of x-ray diffraction if neutral atoms are assumed.

3. Experimental method

3.1. Sample preparation

The GeS_2 glass was prepared from high purity Ge (99.999%) and S ($\geqslant$99.998%) following the procedure outlined in [43]. The elements were weighed in a high purity argon filled glove box in the correct proportions to give a total sample mass of $\approx$3 g and were sealed under a vacuum of $\approx 10^{-5}$ Torr in a cleaned silica ampoule of 7 mm inner diameter and 1 mm wall thickness. The sealed ampoule was heated in a rocking furnace at 1 °C min^{-1} to 950 °C, dwelling at intermediate temperatures of 119 °C (the melting point of sulfur), 445 °C (the boiling point of sulfur) and 937 °C (the melting point of germanium) for 4 h periods, and was maintained at the highest temperature for $\approx$24 h. The furnace was then placed in a vertical position and left for 5 h, cooled to 920 °C at 1 °C min^{-1} and left for 4 h, before the ampoule was rapidly quenched into icy water. The sample ingots thus formed were visibly homogeneous and yellow in colour and there was no deposit left elsewhere on the inside of an ampoule. A glass transition temperature T_g of 514(2) °C (mid-point) was obtained from the reversible part of the heat flow measured using a TA Instruments Q100 modulated differential scanning calorimeter with a scan rate of 3 °C min^{-1}, modulation of $\pm$1 °C per 60 s and an oxygen-free nitrogen gas flow rate of 50 ml min^{-1}. By comparison, the T_g value estimated from the total heat flow takes a smaller mid-point value of 493(3) °C. These results compare with literature values of 453(2) °C [37], $\approx$473 °C [44], $\approx$490 °C [45], 491(5) °C [29], $\approx$495 °C [46] and $\approx$520 °C [47]. Some of this spread in values can be attributed to the method used to measure T_g e.g. the result of [29] was obtained from the total heat flow measured in a differential scanning calorimetry experiment and is in agreement with the present value. A more recent modulated differential scanning calorimetry experiment on GeS_2, using a scan rate of 3 °C min^{-1} with a modulation of $\pm$1 °C per 100 s, gave mid-point T_g values of 508 °C (reversible heat flow) and 489 °C (total heat flow) [48]. Before each diffraction experiment, a glassy sample was extracted from its ampoule and part of it was finely powdered using an agate mortar and pestle.

3.2. Neutron and x-ray diffraction experiments under ambient conditions

The neutron diffraction experiment on glassy GeS_2 was made using the GEM diffractometer at the ISIS pulsed neutron source [49]. The finely powdered sample was held at ambient temperature ($\approx$25 °C) in a cylindrical vanadium can of 4.8 mm internal diameter and 0.1 mm wall thickness and diffraction patterns were taken for the sample in its container, the empty container, the empty instrument, and a vanadium rod of diameter 5.99 mm for normalization purposes. Each complete diffraction pattern was built up from the intensities measured for the different detector groups. These intensities were saved at regular intervals and no deviation between them was observed, apart from the expected statistical variations, which verified the diffractometer stability [51]. The data were analysed using the program GUDRUN [50] which makes the necessary corrections detector by detector before merging the results to give the neutron total structure factor $S_N(k)$. It was checked that $S_N(k)$ obeys the sum-rule relation $\int_0^\infty [S_N(k) - 1]k^2\,dk = -2\pi^2 n_0$ and gives rise to a well-behaved total pair correlation function $G'_N(r)$. This function should oscillate about zero at r values smaller than the distance of closest approach between the centre of two atoms and, when these small r oscillations in $G'_N(r)$ are set to zero, the Fourier back-transform should be in good overall agreement with the original reciprocal space data set [52]. The number density of the glass $n_0 = 0.0359(1)$ Å^{-3} (see figure 1) was taken from Feltz *et al* [26].

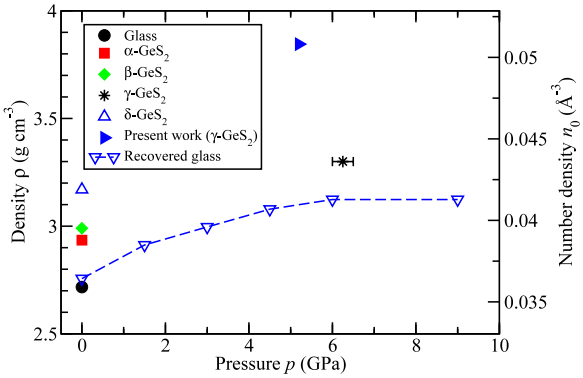

Figure 1. The mass density, ρ, and corresponding number density, n_0, of GeS_2 for the as-prepared glass [26], the high temperature crystalline α phase [22], the low temperature crystalline β phase [23], the crystalline γ phase as prepared at 1100 °C and 6–6.5 GPa and recovered to ambient conditions [70], the high temperature high pressure crystalline δ phase as prepared by a sol-gel process [71], the crystalline γ phase at 5.2(1) GPa and 828(5) K as found in the present work, and the glass for samples that have been pressurized at 1.5, 3, 4.5, 6 or 9 GPa and recovered to ambient conditions [35, 73].

The x-ray diffraction experiment on glassy GeS_2 was made using beamline 11-ID-C at the Advanced Photon Source (APS) with an incident energy of 115.19(6) keV and a single element germanium solid state detector. The loosely packed glass powder was placed in a washer and sealed each side with kapton 77–80 tape to give an approximate slab geometry with a sample thickness of 1.5 mm at the incident beam position. Diffraction patterns were measured for the sample in the kapton container and the empty kapton container. The data were analysed using the ISOMER-X software package which made corrections for the detector deadtime and deviation of the vertical scanning path taken by the detector from a circle centred at the sample position [53]. The atomic form factors were taken from [54] and the Compton scattering correction was taken from [55].

3.3. X-ray diffraction experiments at high pressures and temperatures

The x-ray diffraction experiments were made using the ID30 high pressure beamline of the European Synchrotron Radiation Facility (ESRF) with the Paris–Edinburgh press and sample cell set-up described by Mezouar *et al* [56].

The sample container at the centre of the pressure cell was made from the hexagonal phase of boron nitride (BN) into which finely powdered GeS_2 glass was added. The diffraction measurements were undertaken during two different experimental runs. The first run was made at room temperature at pressures increasing from ambient to ≈5 GPa using a 10 mm gasket with a BN container of outer diameter 2.0 mm and inner diameter 1.5 mm. The second run was made using a 7 mm gasket with the BN container placed in a graphite heater (with a thin gold marker foil) that allowed temperatures in excess of 1000 K to be achieved while maintaining a high pressure. For this run the BN container had inner and outer diameters of 1.4 mm and 2.0 mm, respectively, while the graphite heater had inner and outer diameters of 2.0 and 2.4 mm, respectively. In addition, at the end of the first run, the pressurized sample was recovered to ambient and removed from the cell and a further diffraction pattern was collected for the sample. In all cases the incident beam width was 100 μm. The majority of diffraction experiments were made using an incident wavelength of 0.3311 Å, corresponding to the Ba K-edge (energy of 37.441 keV) used for wavelength calibration. In addition, a few measurements were made at the end of the first run using an incident wavelength of 0.1582 Å, corresponding to the Pt K-edge (energy of 78.395 keV).

The diffraction patterns were collected by using a two-dimensional MAR345 image plate detector and, for the pressure experiments, the large background scattering from the sample cell was minimized by using the ID30 oscillating radial collimator system in the diffracted beam which gave an effective scattered beam width of 100 μm. At each pressure point three measurements of approximately 2 min exposure were made: (i) with the incident beam passing through the centre of the sample, (ii) with the cell moved sideways so that the incident beam passed through the BN sample container, and (iii) with the cell moved further sideways so that the incident beam passed through the gasket material (boron impregnated epoxy). In the case of the high temperature run, a further measurement was made so that the incident beam passed through the graphite heater and Au foil. For the room temperature measurements the pressure in the cell was calculated from the position of the BN (002) peak according to the equation of state given by Le Godec *et al* [57]. The change in temperature and pressure on heating the sample was determined by reference to the position of the BN(002), Au(111) and Au(200) peaks and using the equations of state and thermal expansion coefficients given by Le Godec *et al* [57] for hexagonal BN and by Heinz and Jeanloz [58] and Anderson *et al* [59] for gold.

3.4. X-ray data reduction for high pressure and temperature experiments

The data from the detector were processed using the FIT2D program [60] by first selecting from the image plate only the unobstructed scattering from the sample, i.e. that passing through the collimator but not hitting the sides of the anvils, thus avoiding parasitic scattering from the anvils. The data were at this stage corrected for geometrical effects, such as non-orthogonality of the detector relative to the incident beam, and polarization of the incident beam. FIT2D was then used to integrate the scattered intensity over Debye–Scherrer cones to give a one-dimensional 'powder' pattern of intensity versus scattering angle 2θ [39]. Use of the oscillating radial collimator system enables an elimination of all the container scattering for $2\theta \gtrsim 10°$ and all the gasket scattering for $2\theta \gtrsim 5°$ (see appendix B). The precise scattering angle at which the cut-off occurs depends on the sample diameter and is affected by any distortion that the sample may undergo on compression/heating. The x-ray structure factors were subsequently calculated by using the following analysis procedure.

(i) The diffraction pattern was measured for the sample centred in the incident beam. For this situation, the illuminated volumes of the sample, container and gasket for each scattering angle 2θ were calculated from the known geometry of the incident beam and oscillating radial collimator, and the sample and container diameters (see appendix B).

(ii) The BN container scattering was measured with the cell moved sideways relative to the incident beam. This intensity was scaled, using the calculations made in (i), to be commensurate with the volume of BN illuminated when the sample is positioned so that the incident beam passes through its centre. The scaled container intensity was then subtracted from the intensity measured in stage (i).

(iii) The gasket scattering was also measured with the cell moved sideways relative to the incident beam. This intensity was scaled, using the calculations made in (i), to be commensurate with the volume of gasket illuminated when the sample is positioned so that the incident beam passes through its centre. The scaled gasket intensity was then subtracted from the result of stage (ii). In practice, this additional correction was very small and was not necessary for the ambient temperature run.

(iv) Once the data were corrected for the container and gasket scattering, the resulting intensity was scaled to account for the change in illuminated volume of the sample with scattering angle. A correction was not made for attenuation by the sample, container and gasket materials of the incident and scattered beams (see appendix B).

(v) The resulting data for the sample were normalized to electron units by scaling to match the sum of the self-scattering, $\sum_\alpha c_\alpha f_\alpha(k) f_\alpha^*(k)$, and Compton scattering, $(\mathrm{d}\sigma/\mathrm{d}\Omega)_{\mathrm{Compton}}$, contributions to the x-ray differential scattering cross-section for the sample

$$\left(\frac{\mathrm{d}\sigma}{\mathrm{d}\Omega}\right)_{\mathrm{x}} = \left(\frac{\mathrm{d}\sigma}{\mathrm{d}\Omega}\right)_{\mathrm{Compton}} + \sum_\alpha c_\alpha f_\alpha(k) f_\alpha^*(k) + F(k) \quad (7)$$

where $F(k)$ is defined by equation (1). The Compton scattering corrections were made using the tables given by Hubbell *et al* [61] and the form factors for neutral Ge and S atoms were taken from [54].

In practice the analysis procedure needed to be adjusted because the sample was compressed in the cell, thus reducing its diameter. At each pressure point, this diameter was therefore altered in order to obtain a reasonable fit to the sample self-scattering. Table 1 shows the sample radius used in the

Table 1. The change in effective sample radius with increasing pressure for the diffraction experiment on glassy GeS_2 made using the ID30 high pressure beamline at room temperature.

Applied pressure (GPa)	Effective sample radius (mm)
0.11	0.65
0.75	0.55
1.49	0.53
2.08	0.52
3.07	0.52
3.97	0.52
4.60	0.47
4.96	0.45

analysis at each applied pressure for the ambient temperature run. The x-ray total structure factor $S_X(k)$ at each state point was then obtained by using equation (3) such that

$$S_X(k) - 1 = \frac{(\frac{d\sigma}{d\Omega})_x - (\frac{d\sigma}{d\Omega})_{Compton} - \sum_\alpha c_\alpha f_\alpha(k) f_\alpha^*(k)}{|\langle f(k)\rangle|^2} \quad (8)$$

where $|\langle f(k)\rangle|^2 = \sum_\alpha \sum_\beta c_\alpha c_\beta f_\alpha(k) f_\beta^*(k)$.

3.5. Neutron diffraction experiments using a high pressure set-up

The neutron diffraction experiment on glassy GeS_2 at high pressure and ambient temperature (≈25 °C) was made using a VX5/180 type Paris-Edinburgh (PE) press with two support pillars and standard single toroid anvils [62] made from sintered cubic boron nitride (BN) [63] mounted on the diffractometer D4C [64] at the Institut Laue-Langevin (ILL). An incident wavelength of 0.6960(1) Å was used to optimize the incident flux of neutrons and enabled the use of cadmium (Cd) as an effective shielding material to reduce background scattering. This background scattering was further reduced by using neutron absorbing $^{10}B_4C$ slits placed a few cm upstream of the sample to reduce the vertical divergence of the incident beam. A pellet of finely powdered glass, pre-compacted to the correct geometry, was held in a single toroid gasket made from a Ti–Zr alloy with a mean coherent neutron scattering length of zero. The gasket and collimation provided by the neutron absorbing BN anvils defined a cylindrical sample geometry with the incident and scattered beams in a plane perpendicular to the axis of the cylinder i.e. they both passed through the gasket material. The sample diameter and height under ambient conditions were 6 and 1.6 mm, respectively.

Diffraction patterns were measured for the sample in the gasket with a small applied load (corresponding to an oil pressure of 100 bar applied to a piston of area 66.5 cm^2) to ensure that the gasket took the shape of the anvils (effectively ambient pressure) and at 4.9(5) GPa. The latter was determined from the load applied to the anvils by using a calibration based on many neutron diffraction experiments using crystalline systems with a known equation of state in an otherwise identical set-up (cf [65]). To estimate the container scattering, diffraction patterns were measured for an empty uncompressed (i.e. unsquashed) Ti–Zr gasket and also for several empty Ti–Zr gaskets that had been recovered from different high pressures. To assist in the data normalization at different pressures, diffraction patterns were measured for two differently sized vanadium pellets in an uncompressed or recovered (i.e. pre-squashed) Ti–Zr gasket at ambient pressure. In addition, a diffraction pattern was measured with closed anvils to assist in estimating the background scattering and, to examine the effect of sample self-shielding on the background count rate at small scattering angles [66], diffraction patterns were measured for two differently sized neutron absorbing Cd pellets in an uncompressed or recovered Ti–Zr gasket at ambient pressure. The sample self-shielding correction using Cd was found to be small and, in practice, the correction was not made.

The data reduction followed a procedure [52] where the data collected for the sample were corrected for container and background scattering, taking into account both self-attenuation and multiple scattering effects, and inelasticity corrections were applied. The procedure is not, however, trivial as the scattering geometry changes with pressure (e.g. the sample compresses as the anvils close) and it is not possible to make all of the necessary measurements for the data reduction at each pressure point. The practical details of the data reduction are given by Drewitt *et al* [67].

To make a comparison with the ambient pressure PE press results, the total structure factor for a bulk sample of glassy GeS_2 in a vanadium container (internal diameter 4.8 mm, wall thickness 0.1 mm) was also measured by using D4C under ambient conditions with an incident neutron wavelength of 0.6960(1) Å. The data reduction followed the procedure described elsewhere [52].

4. Results

4.1. Structure of GeS_2 at ambient pressure and temperature by neutron and x-ray diffraction

The total structure factors $S_N(k)$ and $S_X(k)$ measured for glassy GeS_2 under ambient conditions are compared in figure 2 and the first three peak positions are summarized in table 2. Both functions display a well defined FSDP at $k_{FSDP} \simeq 1.02$ Å^{-1} which, by comparison with the measured partial structure factors for glassy [14, 15] and liquid $GeSe_2$ [19, 68], will have a dominant contribution from the Ge–Ge correlations (also see section 5.1). The FSDP is often associated with oscillations of periodicity $2\pi/k_{FSDP}$ in r space whose extent is controlled by the correlation length $2\pi/\Delta k_{FSDP}$ where Δk_{FSDP} is the full width at half maximum of the FSDP [9]. The latter, obtained by reflecting the low k side of the FSDP about its maximum, is 0.37(2) Å^{-1} for $S_N(k)$ and 0.32(2) Å^{-1} for $S_X(k)$ which give a mean correlation length of ≈18 Å.

The total pair distribution functions $G'_N(r)$ and $G'_X(r)$ for glassy GeS_2 under ambient conditions are shown in figure 3 and the first few peak positions and nearest-neighbour coordination number are summarized in table 2. The first peak in these functions at 2.22(2) Å is assigned to Ge–S correlations by comparison with the crystal structures of GeS_2 [22, 23, 69–71]. This assignment assumes the absence of homopolar bonds that are observed in the measured partial pair distribution functions for glassy $GeSe_2$ [14, 15].

Table 2. Several of the parameters describing the structure of glassy GeS_2. The positions k_{FSDP}, k_{PP} and k_3 of the first three peaks in the measured $S(k)$ functions are given together with the positions r_{GeS}, r_{GeGe} and r_3 of the first three peaks in the corresponding $G'(r)$ functions and the Ge–S coordination number $\bar{n}^{S}_{Ge}$ obtained from the first peak in $G'(r)$. The functions were measured using either neutron diffraction (ND) or x-ray diffraction (XRD) and all of the measurements were made at ambient temperature.

$S(k)$			$G'(r)$					
k_{FSDP} (Å^{-1})	k_{PP} (Å^{-1})	k_3 (Å^{-1})	r_{GeS} (Å)	r_{GeGe} (Å)	r_3 (Å)	$\bar{n}^{S}_{Ge}$	Method	Diffractometer
1.03(1)	2.35(1)	3.70(2)	2.22(2)	2.94(2)	3.46(5)	3.97(5)	ND[a]	GEM
1.01(1)	2.30(1)	3.70(2)	2.22(2)	2.94(2)	3.45(2)	4.07(5)	XRD[a]	11-ID-C
1.12(5)	2.20(5)	3.72(5)	2.24(2)	—	3.53(2)	3.9(1)	XRD[b]	ID30
1.03(2)	2.42(5)	3.75(5)	2.21(2)	—	3.46(3)	4.3(2)	ND[a]	D4C
1.12(2)	2.52(5)	3.77(5)	2.20(2)	—	3.42(3)	4.2(2)	ND[c]	D4C

[a] Ambient pressure.
[b] Recovered from 4.96(7) GPa.
[c] *In situ* at 4.9(5) GPa.

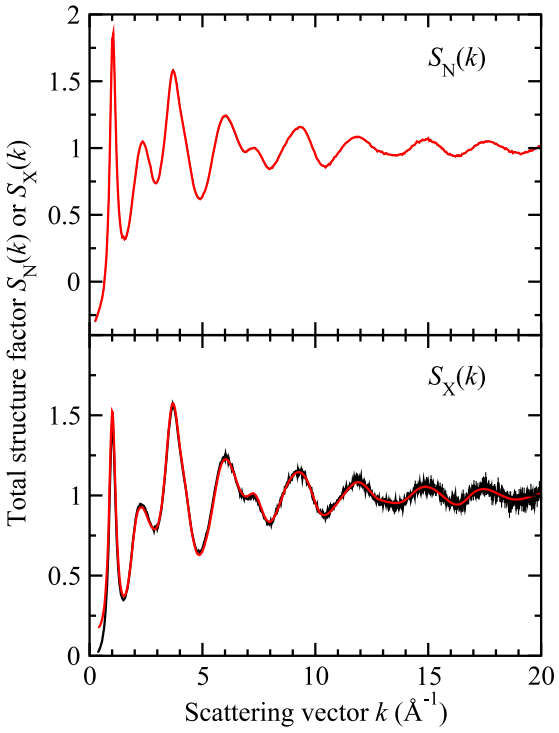

Figure 2. The measured total structure factors $S_N(k)$ and $S_X(k)$ for glassy GeS_2 at ambient temperature (≃25 °C) and pressure as measured by using the neutron diffractometer GEM or the x-ray diffractometer on beamline 11-ID-C. The vertical bars represent the measured data points with statistical errors and the solid (red) curves are the Fourier back-transforms of the corresponding total pair distribution functions $G'_N(r)$ or $G'_X(r)$ given by the solid (black) curves in figure 3 after the unphysical oscillations at r values smaller than the distance of closest approach between the centres of two atoms are set to the calculated $G'_N(r = 0) = G'_X(r = 0) = 0$ limit. In the case of $S_N(k)$ the Fourier back-transform is indistinguishable from the data points at most k values.

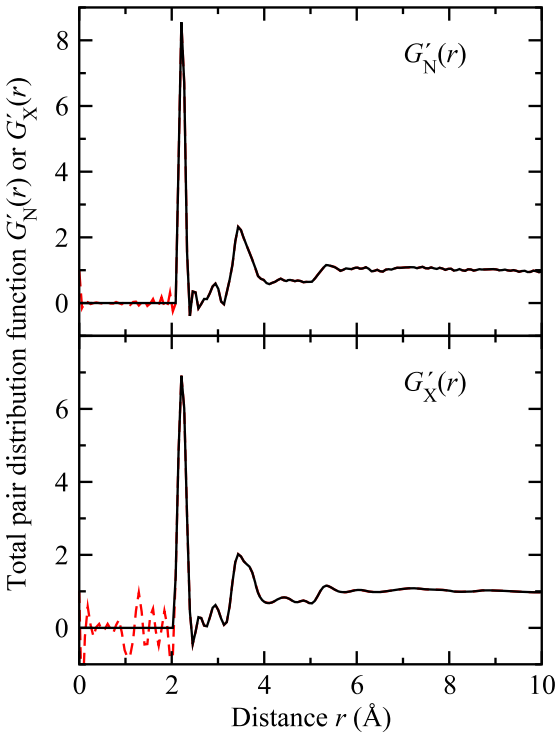

Figure 3. The measured total pair distribution functions for glassy GeS_2 at ambient temperature and pressure. $G'_N(r)$ was obtained by Fourier transforming the $S_N(k)$ function of figure 2 after applying a cosine window function over the range $29.95 \leqslant k$ (Å^{-1}) $\leqslant 34.95$ while $G'_X(r)$ was obtained by Fourier transforming the $S_X(k)$ function of figure 2 after spline fitting and applying a cosine window function over the range $19.975 \leqslant k$(Å^{-1}) $\leqslant 25.575$. The broken (red) curves show the extent of the unphysical small r oscillations.

Integration of the first peak in $G'(r)$ (see appendix A for the method employed in the case of the x-ray data) then gives a coordination number $\bar{n}^{S}_{Ge} = 4.02(5)$ which is consistent with the formation of tetrahedral $Ge(S_{1/2})_4$ motifs. The large measured k range means that a small second peak at 2.94(2) Å in both $G'(r)$ functions can be clearly resolved and this is assigned to Ge–Ge correlations between edge-sharing tetrahedral motifs by comparison with the structure of the high temperature monoclinic α phase of crystalline GeS_2 [22]. This phase forms a layered structure in which chains of Ge centred corner-sharing tetrahedra are cross linked by pairs of Ge centred tetrahedra that share a common edge. There are equal numbers of corner- and edge-sharing tetrahedra and the shortest Ge–Ge distance of 2.92 Å corresponds to the edge-sharing configuration. For the glass, the peak in $G'(r)$ at 2.94 Å is therefore assigned to the distance between the centres of edge-sharing (ES) tetrahedra and integration

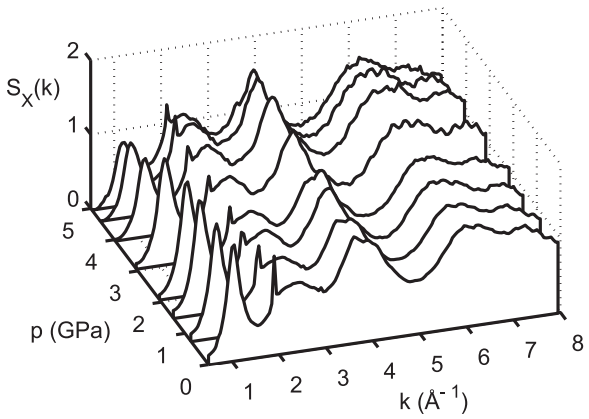

Figure 4. The x-ray total structure factors $S_X(k)$ for glassy GeS_2 at ambient temperature (≃25 °C) and different pressures as measured by using the x-ray diffractometer on beamline ID30. The data sets correspond to pressures of 0.11(2), 0.75(2), 1.49(3), 2.08(3), 3.07(4), 3.97(4), 4.60(5) and 4.96(7) GPa. The Bragg peak at ≈2 $Å^{-1}$ is the remaining contribution from the intense BN (002) reflection that is not completely removed by the correction procedure.

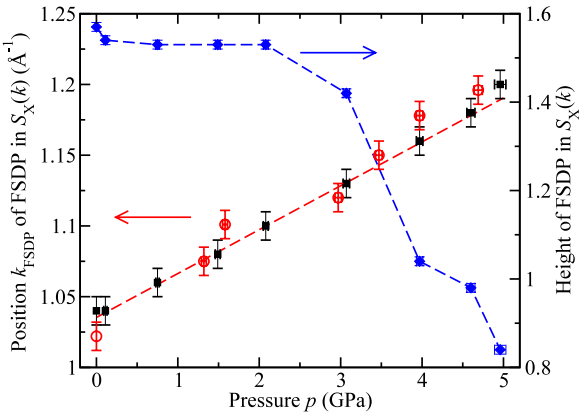

Figure 5. The pressure dependence of the position and height of the first sharp diffraction peak (FSDP) in the total structure factor $S_X(k)$ for glassy GeS_2 at ambient temperature as measured using the x-ray diffractometer on beamline ID30. The vertical and horizontal lines associated with each data point show the error bars. The closed symbols correspond to the measured $S_X(k)$ functions shown in figure 4 and the open (red) symbols correspond to a second experimental run using a smaller sample size (see the text). The light broken (red) curve shows a linear fit to the FSDP positions for a pressure range extending from ambient to 3 GPa and the dark broken (blue) curve is drawn as a guide for the eye.

of the unsmoothed functions gives a coordination number $\bar{n}^{Ge}_{Ge}(ES)$ of 0.46(5) for $G'_N(r)$ and 0.48(5) for $G'_X(r)$. In the high temperature crystalline phase of GeS_2, each Ge atom in an edge-sharing unit has one nearest-neighbour Ge atom in the adjacent edge-sharing unit such that the corresponding coordination number is given by $\bar{n}^{Ge}_{Ge}(ES)$ = [(number of Ge atoms in an edge-sharing tetrahedral unit, $N_{Ge}(ES)) \times 1$]/[total number of Ge atoms in the system, N_{Ge}] i.e.

$$\bar{n}^{Ge}_{Ge}(ES) = \frac{N_{Ge}(ES)}{N_{Ge}} \tag{9}$$

and, since there are equal numbers of Ge atoms involved in corner- and edge-sharing tetrahedra, this expression takes the value of 1/2. Hence if there are no extended chains of edge-sharing units, use of equation (9) for the glass gives a ratio $N_{Ge}(ES)/N_{Ge}$ of 47(5)% which compares with a ratio of 34(5)% for the case of glassy $GeSe_2$ [14, 15]. The third peak in the $G'(r)$ functions at $r_3 \simeq 3.45$ Å will, by comparison with the structure of glassy $GeSe_2$, have a large contribution from Ge–Ge and S–S correlations with a mean S–S distance that is longer than the mean Ge–Ge distance [29]. This assignment is supported by the asymmetry of the third peak e.g. a shoulder appears on the high r side of the third peak in $G'_X(r)$ at ≃3.72(5) Å and a corresponding distance of 3.75(5) Å is estimated from $G'_N(r)$ by peak reflection. If these longer distances are assigned to the S–S distance within Ge centred tetrahedra then the ratio r_{SS}/r_{GeS} is 1.689 for $G'_N(r)$ and 1.676 for $G'_X(r)$ which compares with a value of $\sqrt{8/3} = 1.633$ for regular tetrahedra. Distorted $Ge(S_{1/2})_4$ tetrahedra are a feature in both the low and high temperature phases of crystalline GeS_2 [22, 23]. In addition, the inter-tetrahedral Ge–$\hat{S}$–Ge bond angle, θ_{GeSGe}, can be estimated from the Ge–S and Ge–Ge distances, r_{GeS} and r_{GeGe}, by using the expression $\cos(\theta_{GeSGe}) = 1 - r^2_{GeGe}/2r^2_{GeS}$ [6] whence $\theta_{GeSGe} = 83(1)°$ is obtained for edge-sharing tetrahedra and, by taking $r_{GeGe} = r_3$, $\theta_{GeSGe} = 102(2)°$ is obtained for corner-sharing tetrahedra.

Thus, the neutron and x-ray data for GeS_2 under ambient conditions both point to a model in which the structure is dominated by tetrahedral $Ge(S_{1/2})_4$ motifs in which 47(5)% of the Ge atoms are involved in edge-sharing connections. These motifs link to form a network in which there is intermediate range order, as manifested by the appearance of an FSDP in the measured total structure factors, which has a dominant contribution from the Ge–Ge correlations.

4.2. Pressure dependence of the structure of glassy GeS_2 at ambient temperature by x-ray diffraction

Figure 4 shows the $S_X(k)$ obtained for glassy GeS_2 over the pressure range $0.11(2) \leqslant p(\text{GPa}) \leqslant 4.96(7)$ at room temperature. The measurement at ambient pressure (100 kPa) is not shown for clarity of presentation but is in good agreement with the results reported in section 4.1 showing an FSDP at $k_{FSDP} = 1.03(2)$ $Å^{-1}$. The Bragg peak at ≈2 $Å^{-1}$ is the remaining contribution from the intense BN (002) reflection from the sample cell that was not completely removed by the correction procedure. Figure 5 shows the pressure dependence of k_{FSDP} as determined from a Lorentzian fit. The peak position moves to higher k with increasing pressure, which is consistent with a shortening of the periodicity of the corresponding intermediate range order in real space [9]. The height of the FSDP is also plotted in figure 5 and remains reasonably constant up to a pressure of ≈2 GPa before showing a substantial decrease. This sharp decline is accompanied by a change in the third peak at $k_3 \approx 3.7$ $Å^{-1}$ which becomes notably sharper and displaced to higher k. The observed shift with pressure of the FSDP position to increasing k values, and the decrease in the FSDP height, are consistent with the results obtained by Tanaka [36].

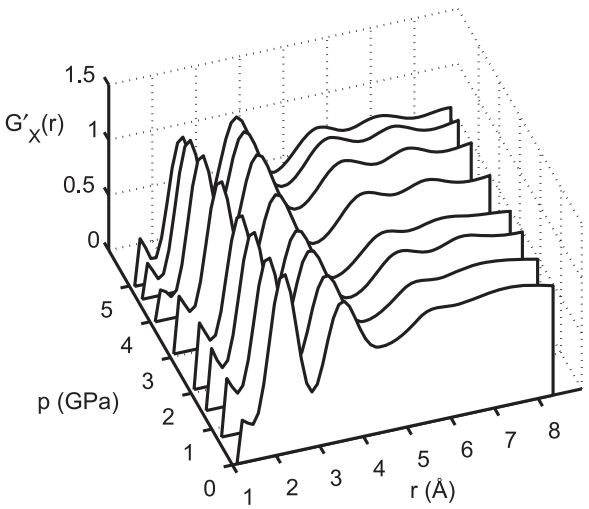

Figure 6. The x-ray total pair distribution functions $G'_X(r)$ for glassy GeS_2 at ambient temperature and different pressures as obtained by Fourier transforming the $S_X(k)$ functions given in figure 4 after the application of a Lorch [41] modification function with $k_{max} \simeq 8$ Å^{-1}. The small peak at ≈1.2 Å is a Fourier transform artefact.

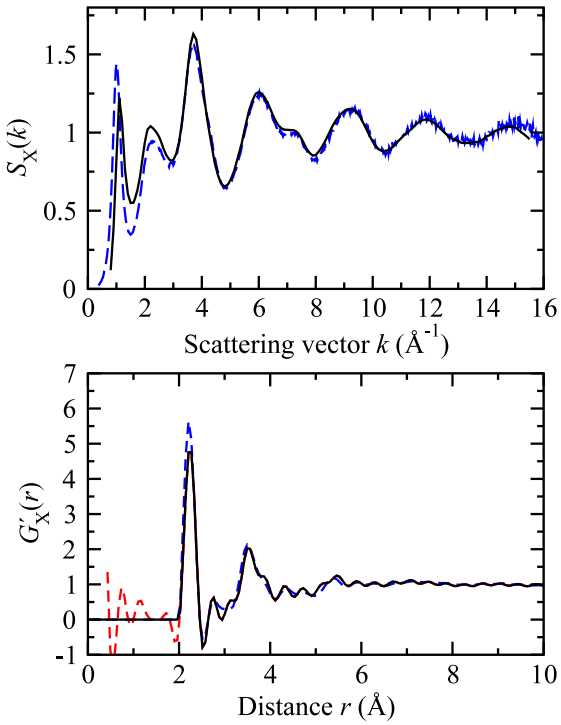

Figure 7. The solid (black) curves give the total structure factor $S_X(k)$ (upper panel) and corresponding total pair distribution function $G'_X(r)$ (lower panel) as measured using the x-ray diffractometer on beamline ID30 for a sample of glassy GeS_2 recovered to ambient conditions after pressurization at 4.96(7) GPa. In the lower panel, the broken (red) curve shows the extent of the unphysical small r oscillations. For comparison, the broken (blue) curve shows $S_X(k)$ for as-prepared GeS_2 under ambient conditions (see figure 2) or the corresponding $G'_X(r)$ as obtained by Fourier transforming $S_X(k)$ after truncating at the same value ($k_{max} = 15.5$ Å^{-1}) as for the ID30 data.

Figure 6 shows the pair distribution functions $G'_X(r)$ obtained from the $S_X(k)$ by using equation (6) with a Lorch [41] modification function. The number densities were estimated from the values measured for permanently densified samples that had been subjected to the same pressure and recovered to ambient conditions [35, 73] (see figure 1). The measured k range was limited to $0.4 \leqslant k(\text{Å}^{-1}) \leqslant 8$ and, in consequence, the peaks in $G'_X(r)$ are broadened considerably and do not give precise positions and intrinsic widths. The first peak in $G'_X(r)$ at ambient pressure is located at $r_{GeS} = 2.18(3)$ Å as compared to 2.22(2) Å reported in table 2. Within the resolution of our data, no change was observed in the position of the first peak with increasing pressure although there was a steady decrease in its height which suggests that some broadening takes place. By integrating under the first peak in $G'_X(r)$ and assuming that it corresponds solely to Ge–S correlations, a coordination number $\bar{n}^S_{Ge} = 4.0(5)$ was obtained by using the method outlined in appendix A. However, the peak width and overlap with the second peak do not allow us to make any observations concerning a change in coordination number with pressure and a peak at ≈2.9 Å associated with edge-sharing tetrahedra could not be resolved. The peaks at 3.57(3) and 5.65(5) Å in $G'_X(r)$ at ambient pressure shift to 3.47(3) and 5.35(5) Å at 4.96 GPa, respectively.

4.3. Structure of glassy GeS_2 recovered from 4.96(7) GPa by x-ray diffraction

At the end of the first experimental run, the pressure was released and the sample was recovered from the pressure cell. The recovered sample was homogeneous and dark brown in colour compared to the yellow colour of the as-prepared sample. This change of appearance is consistent with a red shift in the optical absorption edge in densified and glassy GeS_2 [21, 35, 72]. The recovered sample was mounted on the diffractometer, without the pressure cell and oscillating radial collimator system, and diffraction patterns of the unencumbered sample were acquired for incident wavelengths of 0.3311 and 0.1582 Å to obtain high counting statistics over a wide k range. Several of the parameters describing the structure are listed in table 2 and a number density of $n_0 = 0.041$ Å^{-3} was estimated from the measured density for a GeS_2 glass compacted at 5 GPa and recovered to ambient conditions [35, 73] (see figure 1).

Figure 7 shows the $S_X(k)$ measured for the recovered sample over the range $0.5 \leqslant k(\text{Å}^{-1}) \leqslant 15.5$. The FSDP in $S_X(k)$ is at 1.12(5) Å^{-1} indicating that the glass has not recovered to its original state, in agreement with the experiments on recovered glasses reported by Miyauchi *et al* [35]. The FSDP position corresponds to a pressure of about 3 GPa for the samples studied *in situ* (see figure 5) which may indicate that there are structural similarities between the recovered sample and the glass at this pressure. The corresponding total pair distribution function $G'_X(r)$ is also shown in figure 7. The increased measurement k range gives an improved resolution of the features in $G'_X(r)$. Clearly resolved peaks are found at 2.24(2), 3.53(2) and 5.47(5) Å and there is, perhaps, a shoulder at ≈2.9 Å which suggests the presence of

edge-sharing tetrahedra in the recovered sample. The first peak in $G'_X(r)$ gives a coordination number $\bar{n}^S_{Ge} = 3.9(1)$.

4.4. Structure of GeS_2 at high pressures and high temperatures by x-ray diffraction

In the second experimental run, diffraction patterns were again recorded for glassy GeS_2 as the sample was pressurized from 100 kPa to 4.7(1) GPa at room temperature. Due to the smaller sample size the scattering from the sample container (which now incorporated a graphite heater) and gasket was more significant than for the first run but the results were, nevertheless, consistent. The sample was then heated and remained glassy with no observable change in the FSDP position or height until a pressure of 5.2(1) GPa and a temperature of 828(50) K was obtained. At this point the sample crystallized and examination of the image plate showed significant texturing with some isolated Bragg spots in the Debye–Scherrer rings. It was, however, possible to obtain the crystal structure which is described in section 4.5. A transformation to the same crystal structure, after treatment of the glass at 6 GPa and 873 K, is reported by Miyauchi *et al* [35] although details are not given.

On further heating this crystalline phase was observed to disappear in the powder pattern at 5.1(1) GPa and 1048(50) K. Examination of the image plate showed little evidence of any continuous Debye–Scherrer rings and a large number of individual Bragg spots suggesting that the sample had annealed to form a small number of large and highly oriented crystals. Finally as the temperature of the sample reached 1054(50) K at 4.9(1) GPa virtually all of the Bragg spots had disappeared and a larger diffuse background was observed on the image plate suggesting that the majority of the sample had at this stage melted. Examination of the powder pattern confirmed the underlying liquid-like structure with the first peak at $\approx$2 Å^{-1}. However, there was no evidence of any FSDP at $\approx$1 Å^{-1} as observed in the glass and liquid [74] at ambient pressures. The sample was then quenched at this pressure to ambient temperature in about 5 min and the pressure on the sample was then reduced to $\approx$1.5 GPa. Bragg diffraction from large and highly oriented crystallites was observed on the image plate.

4.5. Structure of crystalline GeS_2 at 5.2(1) GPa and 828(50) K

A set of clearly distinguishable peak positions was located, by taking the second derivative of the intensity $I(2\theta)$ collected *in situ* after devitrification, and the peak profiles were fitted by using a pseudo-Voigt function. The peak positions were automatically indexed, with the wavelength fixed at 0.3311 Å, using CRYSFIRE [75] which gave centred and primitive tetragonal cells with a high figure of merit e.g. the ITO program [76] gave FoM(20) = 93.8 for cell parameters $a = c = 7.0365$ Å, $b = 9.5313$ Å; the TREOR program [77] gave $M(20) = 48$, $F(20) = 127(0.001581, 100)$ for $a = b = 4.9773$ Å, $c = 9.5376$ Å; and the TAUP program [78] gave $F(20) = 28.57$ for an I-centred unit cell with $a = b = 4.9763$ Å, $c = 9.5383$ Å. We proceeded with the smallest cell with highest implied symmetry and used CHEKCELL [79] for space group determination. The best estimated space group, corresponding to the highest number of checked reflections and lowest number of calculated reflections, was $I4_1/amd$. However, we preferred the acentric space group $I\bar{4}2d$ as it gave an equivalent error for only three more calculated reflections. A Le Bail [80] fit in GSAS [81] using 9 fitted parameters (2 cell, 5 background and 2 peak shape parameters) allowed us to refine the cell parameters using this symmetry choice. The fit gave $a = b = 4.97697(17)$ Å and $c = 9.5353(5)$ Å with a cell volume $V = 236.193(17)$ Å^3 which corresponds to a volume per formula unit (f.u.) of $236.193/Z$ or $\approx$59 Å^3 f.u.$^{-1}$ where, considering the density and space group symmetry, Z is most likely equal to 4.

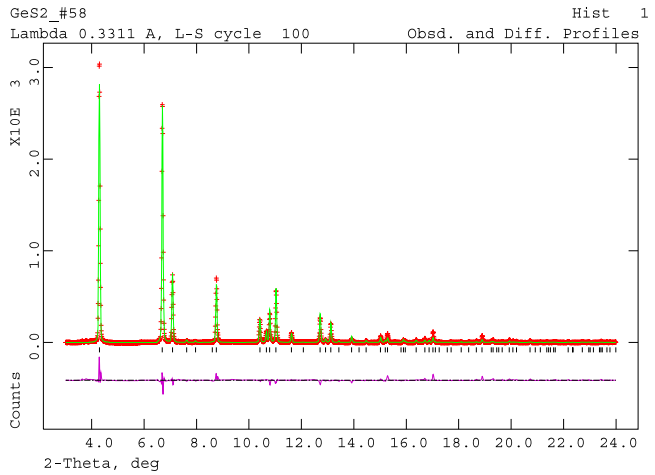

Figure 8. The result of the final Rietveld refinement of x-ray diffraction data, taken for GeS_2 *in situ* at 5.2(1) GPa and 828(50) K, using GSAS with 20 fitted parameters. The measured intensity $I(2\theta)$ is plotted as the ordinate and the scattering angle 2θ is plotted as the abscissa. The (red) crosses represent the measured data points, the solid (green) curve represents the fit, the displaced (purple) curve gives the residual and the vertical markers indicate Bragg peak positions.

We point out that a similar cell and lattice with $I\bar{4}2d$ symmetry has previously been observed by Prewitt and Young [70] for a sample of GeS_2, recovered to ambient conditions after synthesis at high pressure and temperature, and also by Grande *et al* [82] for the selenide analogue $GeSe_2$ as prepared at 3 GPa and 773 K and recovered to ambient conditions. Shimada and Dachille [34] have also reported formation of the Prewitt and Young phase after heat treatment of glassy GeS_2 at 400–500 °C under a pressure in the range 1–5 GPa for a period of 2–4 days. Prewitt and Young [70] described the $I\bar{4}2d$ structure with Ge on a 4*a* site at (0, 0, 0) and S on a 8*d* site at $(x, \frac{1}{4}, \frac{1}{8})$. We used these cell coordinates as initial atomic positions and refined the *in situ* diffraction data using GSAS. The fit gave Rietveld profile reliability factors of $wR_p = 0.1212$ and $R_p = 0.0857$ or, for the data with the background subtracted, $wR_p = 0.1059$ and $R_p = 0.0781$ with reduced $\chi^2 = 0.763$ for 20 fitted parameters. The fitted data are shown in figure 8 and the fitted parameters are summarized in table 3. The region for scattering angles $2\theta = 5.9$–6.5° was excluded from the fit due to the presence of BN (002) and

Table 3. Crystal structure data for GeS_2 at 5.2(1) GPa and 828(50) K as obtained from the final GSAS refinement. The three symbols after Ge and S denote the multiplicity of the Wyckoff position, the Wyckoff letter and site symmetry [87]. The u_{ij} are the refined anisotropic temperature factors. (Space group number 122, $I\bar{4}2d$, has 16 general positions: $(0, 0, 0)+$ and $(\frac{1}{2}, \frac{1}{2}, \frac{1}{2}) + x, y, z; -x, -y, z; y, -x, -z; -y, x, -z; -x + \frac{1}{2}, y, -z + \frac{3}{4}; x + \frac{1}{2}, -y, -z + \frac{3}{4}; -y + \frac{1}{2}, -x, z + \frac{3}{4}; y + \frac{1}{2}, x, z + \frac{3}{4}$.)

Space group			$I\bar{4}2d$ (no 122)
a (Å)			4.97704(12)
c (Å)			9.5355(4)
Volume, V (Å^3)			236.204(12)
Z			4
Formula weight per Z (g)			136.72
Calculated density (g cm^{-3})			3.845
Ge	4	a	$\bar{4}$..
x, y, z	0	0	0
u_{11}, u_{22}, u_{33} (Å^2)	0.0654(9)	0.0654(9)	0.0757(14)
u_{12}, u_{13}, u_{23} (Å^2)	0	0	0
S	8	d	.2.
x, y, z	0.2565(6)	1/4	1/8
u_{11}, u_{22}, u_{33} (Å^2)	0.064(5)	0.145(6)	0.126(4)
u_{12}, u_{13}, u_{23} (Å^2)	0	0	0.041(3)
Overall 2θ range			3°–24°
2θ region excluded from fit			5.9°–6.5°
			BN (002) and graphite (002)
Number of fitted data points			2832
Number of calculated reflections			81

graphite (002) peaks from the container materials (the intensity of both peaks was <10% of the maximum peak intensity).

An analysis using DISAGL [81] shows a 3D structure made from corner-sharing Ge centred tetrahedra (see figure 9) with 4 Ge–S bond lengths of 2.144(2) Å and a S–Ge–S bond angle of 108.00(3)°. The bond angle Ge–S–Ge between adjacent tetrahedra is 106.9(1)°. By comparison, the structure of the recovered material studied by Prewitt and Young [70] had a Ge–S bond length of 2.2123 Å with S–Ge–S and Ge–S–Ge bond angles of 105.7° and 107.5°, respectively. The nearest-neighbour bonds are therefore shortened and the tetrahedra are more regular at high pressure and temperature whereas the angle between adjacent tetrahedra is slightly more distorted. The structure is of the SiS_2-type which is shared by α-$ZnCl_2$ [83–85] and $GeSe_2$ [82]. The calculated density of the high pressure and temperature phase, $\rho = 3.845$ g cm^{-3}, is ≈30% greater than the monoclinic phases of GeS_2 [22, 23] where $V/Z = 75.8$ Å^3 f.u.$^{-1}$ for the Pc structure and 77.3 Å^3 f.u.$^{-1}$ for the high temperature $P2_1/c$ structure. It is also 20% greater than that of the expanded tetragonal structure for GeS_2 reported by MacLachlan *et al* [71] ($ZnBr_2$-type structure with $V/Z = 71.6$ Å^3 f.u.$^{-1}$) and approximately 16% more compressed than the ambient determination of the same SiS_2-type structure by Prewitt and Young [70].

We note that $GeSe_2$ has shown evidence for other 3D structures in tetragonal subgroups of $I\bar{4}2d$ [86] under high pressure and temperature conditions. These structures are extremely difficult to distinguish from the $I\bar{4}2d$ structure by powder diffraction methods. Any distortion due to lowering of the site symmetry is minute and, consequently, any breaking of the $00l$: $l = 4n$ or hkl: $h + k + l = 2n$ reflection conditions for the $I\bar{4}2d$ space group [87] will lead to peaks with very small diffraction intensities (e.g. the (002) reflection for the $I\bar{4}$ (and $P\bar{4}$) structure or the (003) reflection for the $P\bar{4}$ structure). Despite having no evidence for these reflections, we considered it prudent to refine the experimental data for GeS_2 using the parameters given by Grzechnik *et al* [86] with our previously refined tetragonal cell parameters as initial values. The resulting fits gave an improvement by ≈1% in the Rietveld profile reliability factors but there was an increase in the number of fitting parameters and the refinement led to

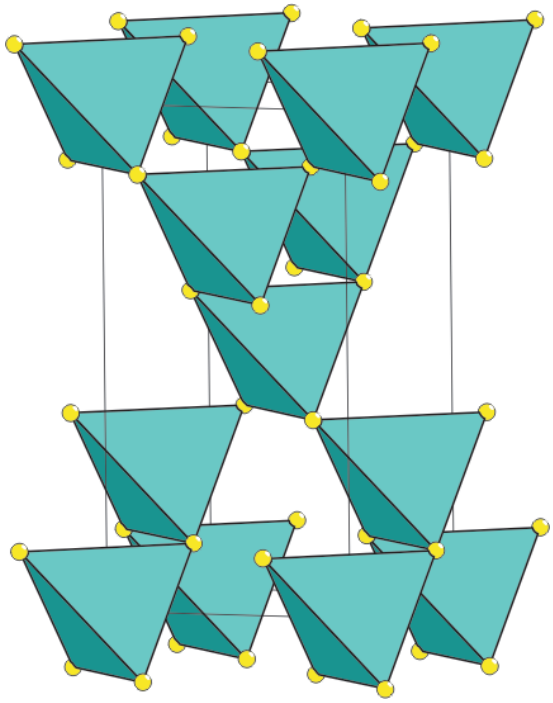

Figure 9. Polyhedral representation of the $I\bar{4}2d$ structure for GeS_2, with the c-axis vertical, showing the corner-sharing linkages between adjacent Ge centred tetrahedra.

short Ge–S bond lengths <2.0 Å. We therefore prefer our assignment of the $I\bar{4}2d$ structure for GeS_2 at 5.2(1) GPa and 828(50) K.

4.6. Pressure dependence of the structure of glassy GeS_2 at ambient temperature by neutron diffraction

The total structure factors $S_N(k)$ measured for glassy GeS_2 in the PE press on D4C at ambient pressure and at 4.9(5) GPa are illustrated in figure 10. In the correction procedure the number density of the glass was taken to be 0.0359(1) $Å^{-3}$ at ambient pressure [26] and was estimated to be 0.0436 $Å^{-3}$ at 4.9 GPa from the density measured by Prewitt and Young [70] (see figure 1). Several of the parameters describing the structure are listed in table 2. In figure 10 the data are compared with the $S_N(k)$ function measured in the present work for a bulk sample of GeS_2 at ambient pressure using the same neutron diffractometer D4C with the same incident neutron wavelength. The ambient pressure $S_N(k)$ function measured with the PE press shows some troughs/peaks at ≈2.70 and 4.85 $Å^{-1}$ and other features that result from an incomplete subtraction of the Ti–Zr gasket scattering (the empty gasket used for the container measurement at ambient pressure was not identical to the gasket used for the sample run). Nevertheless, the ambient pressure data sets are in agreement within the experimental error at most k values and the FSDP position at 1.03(2) $Å^{-1}$ is in agreement with the results given in section 4.1, indicating that the method used to pre-compress the powder pellet for the PE press had little effect on the structure of the illuminated portion of the glass. With pressure increasing to 4.9 GPa, the FSDP moves to 1.12(2) $Å^{-1}$ and its intensity decreases significantly, whereas the third peak moves from 3.75(5) to 3.77(5) $Å^{-1}$ and its intensity increases. The data therefore follow the same trends with increasing pressure that were reported for the measured $S_X(k)$ functions in section 4.2. As found in the x-ray diffraction experiment of section 4.3, the recovered sample was dark brown in colour.

Figure 11 shows the total pair distribution functions $G'_N(r)$ measured *in situ* for glassy GeS_2 at ambient pressure and at 4.9(5) GPa while table 2 lists several of the corresponding parameters. The data are compared with the $G'_N(r)$ function measured for a bulk GeS_2 sample at ambient pressure, obtained by Fourier transforming the $S_N(k)$ function shown in figure 10 with the same cut-off value $k_{max} = 15.45$ $Å^{-1}$. This k range is too small to enable the Ge–Ge correlations for edge-sharing tetrahedra to be resolved at ≈2.9 Å. The nearest-neighbour Ge–S distance and coordination number show little change as the pressure is increased to 4.9 GPa while the peak initially at $r_3 = 3.46(3)$ Å broadens and shifts to a smaller distance of 3.42(3) Å.

We note that the value obtained for the coordination number $\bar{n}^S_{Ge}$ at high pressure depends on the value used for the number density in the data analysis procedure. For example, if $n_0 = 0.051$ $Å^{-3}$ corresponding to the density measured in the present work for crystalline GeS_2 at high pressure and high temperature (see section 4.5), then the data corrections

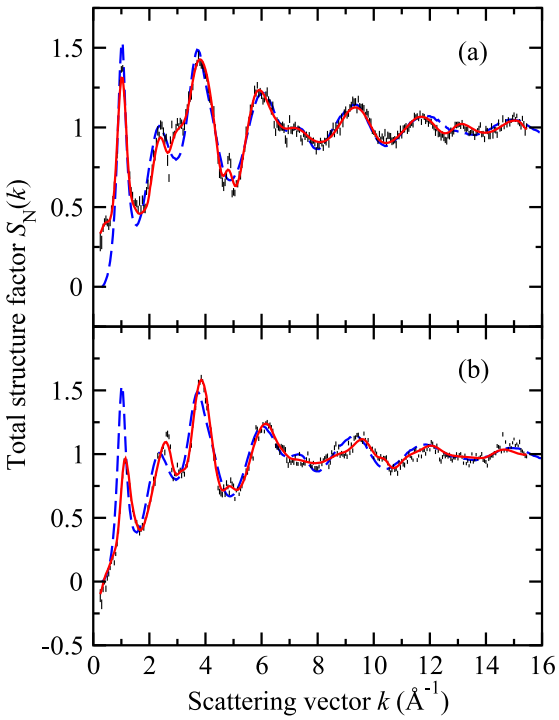

Figure 10. The total structure factors $S_N(k)$ for glassy GeS_2 at ambient temperature (≃25 °C) as measured by using the neutron diffractometer D4C with the Paris-Edinburgh press at either (a) ambient pressure or (b) 4.9(5) GPa. The vertical bars represent the measured data points with statistical errors, and the solid (red) curves are the Fourier back-transforms of the corresponding total pair distribution functions $G'_N(r)$ given by the solid (black) curves in figure 11 after the unphysical oscillations at r values smaller than the distance of closest approach between the centres of two atoms are set to the calculated $G'_N(r = 0) = 0$ limit. For reference, the $S_N(k)$ function measured for a bulk sample of GeS_2 under ambient conditions by using the same neutron diffractometer D4C with the same incident wavelength is given by the broken (blue) curve in both (a) and (b) (see the text).

change and a higher coordination number $\bar{n}^S_{Ge} = 4.9(2)$ is obtained. This coordination number does, however, correspond to an unchanged Ge–S bond length of 2.20(2) Å whereas an increase in bond length with an increase of coordination number is anticipated since the radius of the Ge nearest-neighbour coordination shell should lengthen to accommodate additional S atoms.

5. Discussion

5.1. Structure of glassy GeS_2 under ambient conditions

The results for the structure of glassy GeS_2 under ambient conditions can be readily discussed by comparing the measured total structure factors, $S_N(k)$ and $S_X(k)$, and corresponding total pair distribution functions, $G'_N(r)$ and $G'_X(r)$, with their reconstruction from the measured partial pair correlation functions for glassy $GeSe_2$ [14, 15]. The comparison of the reciprocal space data sets in figure 12 shows that the main features of the total structure factors are reproduced from the measured $S_{\alpha\beta}(k)$ for $GeSe_2$. The dominant contribution to the FSDP in both $S_N(k)$ and $S_X(k)$ arises from the Ge–Ge

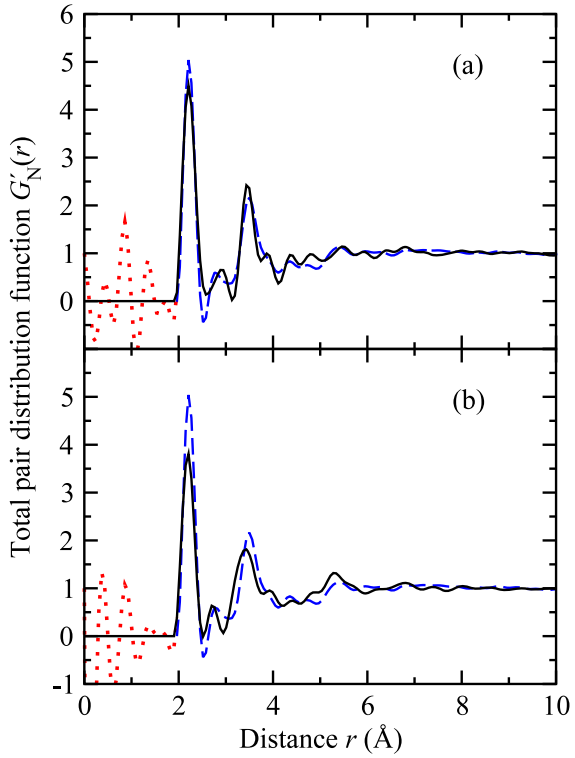

Figure 11. The total pair distribution functions $G'_N(r)$ (solid (black) curves) for glassy GeS_2 at ambient temperature as measured by using D4C with the Paris-Edinburgh press at either (a) ambient pressure or (b) 4.9(5) GPa. In (a) $G'_N(r)$ was obtained by Fourier transforming the $S_N(k)$ function of figure 10(a) after spline fitting and in (b) $G'_N(r)$ was obtained by Fourier transforming the $S_N(k)$ function of figure 10(b) after spline fitting and applying a cosine window function over the range $13.95 \leqslant k(\text{Å}^{-1}) \leqslant 15.45$. The dotted (red) curves show the extent of the unphysical low r oscillations. For reference, the $G'_N(r)$ function measured for a bulk sample of GeS_2 under ambient conditions is given by the broken (blue) curve and was obtained by Fourier transforming the corresponding $S_N(k)$ given in figure 10 after truncation at the same maximum k value as the PE press data.

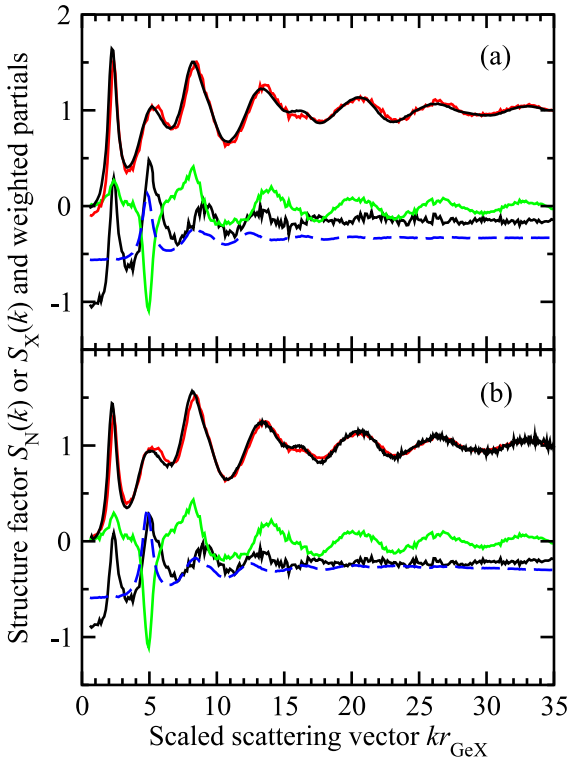

Figure 12. Reconstruction of the measured total structure factors (a) $S_N(k)$ and (b) $S_X(k)$ for glassy GeS_2 under ambient conditions from the measured partial structure factors for glassy $GeSe_2$ [14, 15]. In (a) the upper solid dark (black) curve gives the $S_N(k)$ function measured by Petri and Salmon [29] plotted against the scaled scattering vector kr_{GeS} with $r_{GeS} = 2.21$ Å. The upper solid light (red) curve gives the reconstruction of $S_N(k)$ from the sum of the three weighted partial structure factors measured for glassy $GeSe_2$ where $c^2_{Ge} f_{Ge}(k)^2 S_{GeGe}(k)/\langle f(k)\rangle^2$ (solid dark (black) curve), $2c_{Ge}c_S f_{Ge}(k) f_S(k) S_{GeSe}(k)/\langle f(k)\rangle^2$ (solid light (green) curve) and $c^2_S f_S(k)^2 S_{SeSe}(k)/\langle f(k)\rangle^2$ (broken (blue) curve) and their sum are all plotted against kr_{GeSe} with $r_{GeSe} = 2.36$ Å. The three weighted partial structure factors are displaced vertically by -0.5 for clarity of presentation. The measurements for GeS_2 and $GeSe_2$ were made using the same neutron diffractometer (D4B) with the same incident wavelength. The curves in (b) have the same identity as in (a) except that the upper solid dark (black) curve gives the $S_X(k)$ function measured in the present work (see figure 2) and $r_{GeS} = 2.22$ Å. In (a) the $f_\alpha(k)$ represent the (k-independent) coherent neutron scattering lengths [42] and in (b) they represent the x-ray form factors [54].

correlations and there is also a small contribution from the Ge–S correlations. The principal peak is relatively small owing to a near cancellation of peaks in $S_{GeGe}(k)$ and $S_{SS}(k)$ by a trough in $S_{GeS}(k)$. In real space (figure 13), the first peak in $G'(r)$ is dominated by nearest-neighbour Ge–S correlations and the peak from the Ge–Ge distance in edge-sharing tetrahedra is not particularly pronounced owing to the Fourier transform artefacts that arise from the small k_{max} value. The next peak in $G'(r)$ has a contribution from both Ge–Ge and S–S correlations with a shorter mean Ge–Ge distance.

The peak positions and coordination numbers obtained from the present work (section 4.1 and table 2) are consistent with other studies. For example, previous neutron diffraction work gives an FSDP at 1.02–1.04 Å^{-1} [29, 88] with a principal peak at 2.35(2) Å^{-1} [29]. In real space, most neutron and x-ray diffraction and extended x-ray absorption fine structure (EXAFS) studies give a nearest-neighbour Ge–S distance of 2.21–2.23 Å with a corresponding coordination number $\bar{n}^S_{Ge} \simeq 4$ [26, 28, 29, 89–91]. The Ge–Ge distance for edge-sharing tetrahedra is reported to be in the range 2.89–2.95 Å [28, 90, 91] and the corresponding coordination number $\bar{n}^{Ge}_{Ge}(ES)$ is quoted to be 0.30(6) [90], 0.44(3) [91] or 0.50(3) [28] where the value of $\bar{n}^{Ge}_{Ge}(ES) = 0.44(3)$ was obtained from neutron diffraction results in which the edge-sharing Ge–Ge peak could be resolved in the real space total pair correlation function [91]. The next longest Ge–Ge distance is reported to be in the range from 3.44(2) [90] to 3.47(2) Å [28] as compared to the value of 3.45(2)–3.46(5) Å obtained in the present work. Raman and Mössbauer spectroscopic studies point to the existence of Ge–Ge and S–S homopolar bonds [44, 48, 92] (although the presence of Ge–Ge bonds has recently been disputed [93]) but they appear as a small fraction of the total number of heteropolar Ge–S bonds [29, 48].

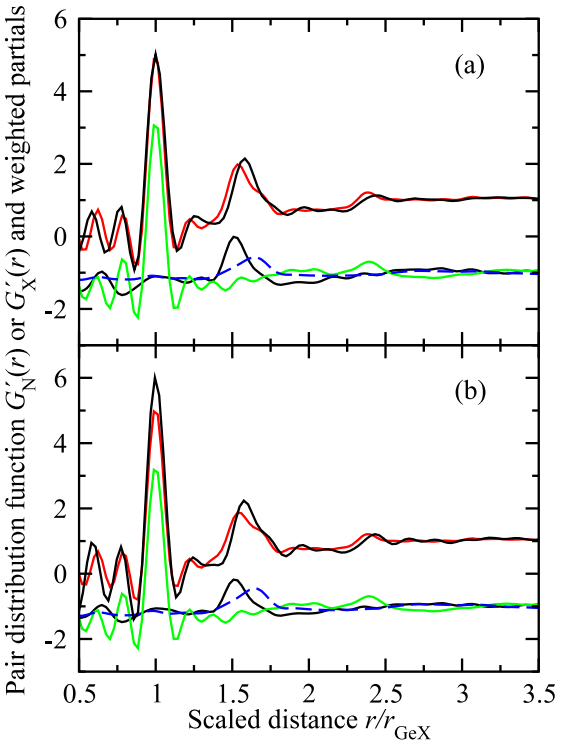

Figure 13. Reconstruction of the measured total pair distribution functions (a) $G'_N(r)$ and (b) $G'_X(r)$ for glassy GeS_2 under ambient conditions from the measured partial pair distribution functions for glassy $GeSe_2$ [14, 15]. In (a) the upper solid dark (black) curve gives the $G'_N(r)$ function measured by Petri and Salmon [29] plotted against the scaled distance r/r_{GeS} with $r_{GeS} = 2.21$ Å. The upper solid light (red) curve gives the reconstruction of $G'_N(r)$ from the sum of the three weighted partial pair distribution functions measured for glassy $GeSe_2$, as obtained by Fourier transforming the weighted Ge–Ge (solid dark (black) curve), Ge–Se (solid light (green) curve) and Se–Se (broken (blue) curve) partial structure factors given in figure 12(a), where all four functions are plotted against r/r_{GeSe} with $r_{GeSe} = 2.36$ Å. The three weighted partial pair distribution functions are displaced vertically for clarity of presentation. The curves in (b) follow the labelling in (a) except that the upper solid dark (black) curve gives the $G'_X(r)$ function obtained in the present work by Fourier transforming $S_X(k)$ given in figure 2 (after truncation at $k_{max} = 15.9$ Å^{-1} to match the limit used in [29]) and $r_{GeS} = 2.22$ Å. The agreement between $G'(r)$ and its reconstruction from the $g_{\alpha\beta}(r)$ for $GeSe_2$ in the region of the peak at $r/r_{GeX} \simeq 1.55$ can be improved by using the weighted $g_{GeGe}(r)$ and $g_{SeSe}(r)$ functions as plotted against the scaled distances r/r_{GeGe} and r/r_{SeSe}, respectively, where r_{GeGe} and r_{SeSe} are the nearest-neighbour (homopolar) bond lengths [29].

5.2. *Structure of GeS_2 under pressure*

On pressurizing glassy GeS_2 to $\simeq$5 GPa at ambient temperature, the most dramatic changes observed in $S_X(k)$ and $S_N(k)$ are a steady shift in position of the FSDP to larger k values and, on increasing the pressure beyond $\approx$2 GPa, a rapid reduction of the FSDP height (see figures 4 and 5). As shown in figure 12, this can be attributed to a change in the intermediate range order associated with the Ge–Ge correlations i.e. to a reorganization in the arrangement of $Ge(S_{1/2})_4$ tetrahedra. The real space results do not show a change in position of the first peak in $G'_X(r)$ or $G'_N(r)$ with increasing pressure but the peak at $\simeq$3.45 Å does move to a smaller distance and the peak at $\simeq$5.4 Å shifts to $\simeq$5.3 Å (see figure 11). The consistency in value of the nearest-neighbour Ge–S distance and corresponding coordination number $\bar{n}^S_{Ge} \simeq 4$ leads to the conclusion that the local tetrahedral motifs remain intact at pressures up to $\simeq$5 GPa. The reconstruction of the $G'(r)$ functions from the measured partial pair distribution functions for glassy $GeSe_2$ shows that the shift in the peak at $\simeq$3.45 Å to small r is most likely associated with the Ge–Ge correlations (figure 13) and therefore with the change in properties of the FSDP with increasing pressure. This shift might arise from a lengthening of the short Ge–Ge distances in edge-sharing tetrahedra as they transform to corner-sharing motifs and/or a decrease in the Ge–S–Ge angle between corner-sharing tetrahedra. However, the mean Ge–S–Ge bond angle of 102(3)° estimated from the peak positions r_{GeS} and r_3 measured by neutron diffraction for the glass at 4.9(5) GPa (see table 2) does not appear to have changed from its ambient pressure value (see section 4.1). This may result from an increasing overlap with pressure between the nearest-neighbour Ge–Ge and S–S correlations that renders unsafe the assignment of r_3 solely to Ge–Ge correlations. The peak initially at $\simeq$5.4 Å arises from the Ge–S correlations (figure 13). On recovering the glass from $\simeq$5 GPa to ambient, the comparison of figure 7 suggests that the local ordering is restored, although there is perhaps a small elongation of the Ge–S bond length to 2.24(2) Å, but the intermediate range order remains permanently changed as shown by the shift in position and intensity of the FSDP (table 2). A hysteresis in the pressure dependence of the optical properties of glassy GeS_2 is also observed [21, 72]. On heating the glass at $\simeq$5 GPa, the system crystallizes to form a 3D structure comprising corner-sharing $Ge(S_{1/2})_4$ tetrahedra (see figure 9).

EXAFS results for glassy GeS_2 samples, pressurized to 6 GPa and recovered to ambient conditions, show an increase in the Ge–S bond distance from 2.224(1) to 2.231(1) Å while the coordination number remains at $\bar{n}^S_{Ge} \simeq 4$, an observation that is supported by complementary x-ray diffraction and Raman spectroscopy studies [35]. X-ray diffraction and sulfur K-edge x-ray absorption near edge structure (XANES) studies of the densified samples suggest a reduction in the number of edge-sharing Ge–Ge configurations with increasing applied pressure [35]. *In situ* EXAFS studies of glassy GeS_2 show a reduction of the Ge–S bond length from 2.225 Å at ambient pressure to 2.200 Å at 8 GPa while annealing at this elevated pressure at 270 °C leads to a small elongation of the bond length to 2.205 Å [94]. On recovery to ambient conditions, the final bond length of 2.234 Å was longer than the initial bond length, in agreement with earlier observations made by the same authors [35]. During this treatment of the glass the Ge–S coordination number remained more-or-less the same at $\bar{n}^S_{Ge} \simeq 4$. The increase in the Ge–S bond length on recovery to ambient conditions was attributed to a change in competition between ordering on the local and intermediate atomic length scales [94].

Raman spectroscopy experiments on glassy GeS_2 under hydrostatic conditions at 300 K show a shift of the A_1 mode, which is assigned to the symmetric breathing vibrations

of S atoms in corner-sharing $Ge(S_{1/2})_4$ tetrahedra, from 342(1) cm^{-1} at ambient pressure to a higher frequency of 358(4) cm^{-1} at 10.8 GPa [95, 96]. This shift is attributed to a decrease of the Ge–S bond length with increasing pressure. The companion A_1^c mode in the ambient pressure spectra at $\simeq$374 cm^{-1}, which is assigned to the symmetric stretching vibrations of S atoms in the bridges of edge-sharing $Ge(S_{1/2})_4$ tetrahedra, no longer appears as a distinct feature at a pressure $\approx$6 GPa. The A_1^c mode does, however, reappear when the glass is recovered to ambient conditions from 10.8 GPa [95]. Similar observations were made by Weinstein and Slade [97] for glassy GeS_2 under hydrostatic conditions at 13 K and pressures up to 5.6 GPa. These authors also investigated the pressure induced peak broadening.

Raman scattering and optical absorption spectra for the high temperature crystalline monoclinic α phase of GeS_2 at 300 K under hydrostatic conditions indicate a phase transition at $\approx$9 GPa [98] to the tetragonal γ phase of Prewitt and Young [70] i.e. the edge-sharing $Ge(S_{1/2})_4$ tetrahedra in the two-dimensional layered crystal structure of the α phase transform into corner-sharing $Ge(S_{1/2})_4$ tetrahedra in the three-dimensional structure of the γ phase. A further transition with increasing pressure takes place at $\approx$15 GPa to a highly disordered (possibly amorphous) phase [98]. In the case of the low temperature crystalline monoclinic β phase, similar measurements show a phase change at 11.0(5) GPa into an unknown structure [21].

5.3. Comparison between the structures of glassy GeS_2 and $GeSe_2$ under pressure

The structure of glassy $GeSe_2$ with pressure increasing to 9.3 GPa has been investigated by *in situ* x-ray diffraction at ambient temperature [16]. The FSDP at $k_{FSDP} = 1.010(5)$ $Å^{-1}$ at ambient pressure shifts to higher k values with increasing pressure and its intensity decreases so that the peak almost disappears by 9.3 GPa. In comparison, the principal peak that is initially at 2.042(5) $Å^{-1}$ shifts to 2.262(5) $Å^{-1}$ and its height increases. In real space, the mean Ge coordination number increases from 4.0(2) at a mean distance of 2.364(5) Å to 4.5(2) at a mean distance of 2.376(5) Å as the pressure is increased from ambient to 9.3 GPa and the peak initially at 3.90(1) Å in $rG'_X(r)$ broadens and shifts to 3.62(2) Å. The results are consistent with the occurrence of two densification processes, namely a conversion from edge-sharing to corner-sharing $Ge(Se_{1/2})_4$ tetrahedra and a gradual increase in the mean coordination number with increasing density. A competition between these mechanisms is attributed to a minimum in the network rigidity at about 3 GPa [99]. A decrease in the number of edge-sharing motifs relative to corner-sharing motifs with pressure increasing to $\approx$3 GPa is supported by Raman spectroscopy results [100].

The results for glassy $GeSe_2$ can be readily discussed by comparing the measured total structure factors, $S_N(k)$ and $S_X(k)$, and corresponding total pair distribution functions, $G'_N(r)$ and $G'_X(r)$, with their reconstruction from the measured partial pair correlation functions for this material under ambient conditions [14, 15]. By contrast to GeS_2, the neutron

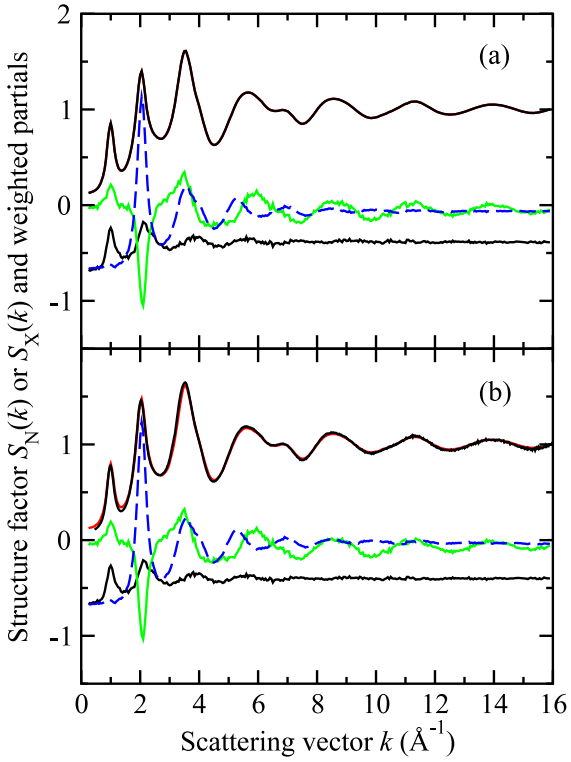

Figure 14. Reconstruction of the measured total structure factors (a) $S_N(k)$ and (b) $S_X(k)$ for glassy $GeSe_2$ under ambient conditions from the measured partial structure factors for this material [14, 15]. In (a) the upper solid dark (black) curve gives the $S_N(k)$ function measured by Petri *et al* [14, 15] for a $GeSe_2$ sample containing Ge and Se of natural isotopic abundance. The upper solid light (red) curve gives the reconstruction of $S_N(k)$ from the sum of the three weighted partial structure factors $c_{Ge}^2 f_{Ge}(k)^2 S_{GeGe}(k)/\langle f(k)\rangle^2$ (solid dark (black) curve), $2c_{Ge}c_{Se}f_{Ge}(k)f_{Se}(k)S_{GeSe}(k)/\langle f(k)\rangle^2$ (solid light (green) curve) and $c_{Se}^2 f_{Se}(k)^2 S_{SeSe}(k)/\langle f(k)\rangle^2$ (broken (blue) curve). The $S_N(k)$ function and partial structure factors were all measured as part of the same experiment using the same neutron diffractometer (D4B) so that the total structure factor and its reconstruction are identical. The three weighted partial structure factors are displaced vertically by −0.5 for clarity of presentation. The curves in (b) have the same identity as in (a) except that the upper solid dark (black) curve gives the $S_X(k)$ function measured using 11-ID-C following the procedure described in section 3.2 (the glass was prepared using the method given in [15]). In (a) the $f_\alpha(k)$ represent the (k-independent) coherent neutron scattering lengths [42] and in (b) they represent the x-ray form factors [54].

scattering length for Se ($b_{Se} = 7.970(9)$ fm cf $b_S = 2.847(1)$ fm [42]) and its atomic form factor ($f_{Se}(k) = 34$ cf $f_S(k) = 16$ electron units at $k = 0$) are much larger than for S which gives an increased weighting factor for those correlations involving the chalcogen atom.

In reciprocal space, the comparison of figure 14 shows that the FSDP in both $S_N(k)$ and $S_X(k)$ has an almost equal contribution from the Ge–Ge and Ge–Se correlations i.e. it is not dominated by the Ge–Ge correlations as in the case of GeS_2 (figure 12) which accounts for its smaller relative height. By comparison, the larger weighting given to the Se–Se correlations leads to a relatively intense principal peak at $\simeq$2.04 $Å^{-1}$. The changes with pressure associated with the FSDP in $GeSe_2$ are therefore related to an alteration of

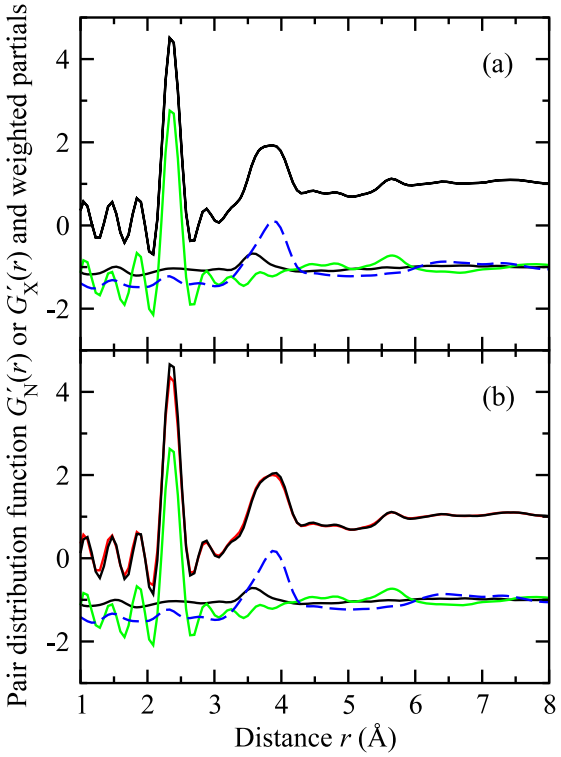

Figure 15. Reconstruction of the measured total pair distribution functions (a) $G'_N(r)$ and (b) $G'_X(r)$ for glassy $GeSe_2$ under ambient conditions from the measured partial pair distribution functions for this material [14, 15]. In (a) the upper solid dark (black) curve gives the $G'_N(r)$ function obtained by Fourier transforming the $S_N(k)$ function of figure 14(a) and the upper solid light (red) curve (which in this case is indistinguishable from the upper solid dark (black) curve) gives the reconstruction of $G'_N(r)$ from the sum of the three weighted partial pair distribution functions obtained by Fourier transforming the weighted Ge–Ge (solid dark (black) curve), Ge–Se (solid light (green) curve) and Se–Se (broken (blue) curve) partial structure factors given in figure 14(a). The three weighted partial pair distribution functions are displaced vertically for clarity of presentation. The curves in (b) follow the labelling in (a) except that the upper solid dark (black) curve gives the $G'_X(r)$ function obtained in the present work by Fourier transforming $S_X(k)$ given in figure 14(b) after truncation at $k_{max} = 15.9$ Å^{-1} to match the limit used in [14, 15].

the intermediate range order associated with Ge correlations. These changes do occur, however, at a slower rate by comparison with glassy GeS_2 which suggests a concomitant slower rate for the structural reordering. For example, the rate of change of the FSDP position is $\simeq$0.023 Å^{-1} GPa^{-1} for $GeSe_2$ [16] and $\simeq$0.031 Å^{-1} GPa^{-1} for GeS_2 (see figure 5). Also, an extrapolation of the FSDP height for GeS_2 in figure 5 suggests that this peak would finally disappear at $\approx$7.8 GPa, a pressure lower than the 9.3 GPa for which an FSDP in $GeSe_2$ still remains. In real space, the comparison of figure 15 shows that the Se–Se correlations within tetrahedral motifs give the major contribution to the peak at $\simeq$3.9 Å and will therefore dominate the shifts observed in the second peak with increasing pressure. This contrasts with the case of glassy GeS_2 where the Ge–Ge and S–S correlations have an almost equal weighting (figure 13).

6. Conclusions

Germanium disulfide provides an excellent test bed for investigating the nature of structural transformations in chalcogenide materials. The *in situ* x-ray and neutron diffraction studies show that the glass structure is based on $Ge(S_{1/2})_4$ tetrahedra at pressures up to $\simeq$5 GPa and that the position of the second peak in $G'(r)$, which has a large contribution from Ge–Ge correlations, reduces with increasing pressure. The latter may result from a lengthening of short Ge–Ge distances in edge-sharing tetrahedra as they transform to corner-sharing tetrahedra and/or a decrease in the Ge–$\hat{S}$–Ge inter-tetrahedral bond angle between corner-sharing motifs. A conversion from edge-sharing to corner-sharing tetrahedra with increasing pressure is suggested by other x-ray diffraction and XANES studies [35] and the A_1^c mode in Raman spectra, which is a signature of edge-sharing tetrahedra, no longer appears as a distinct feature at $\approx$6 GPa [95]. A conversion from edge-sharing to corner-sharing tetrahedra with increasing pressure is reported for glassy $GeSe_2$ [16, 100]. With increasing temperature at a pressure of $\simeq$5 GPa, the GeS_2 system crystallizes to form the tetragonal space group $I\bar{4}2d$ wherein corner-sharing $Ge(S_{1/2})_4$ tetrahedra pack to form a dense 3D network. It is notable that of the GeS_2 crystalline polymorphs, the structure with the smallest density corresponds to the 2D α phase which contains edge-sharing motifs (see figure 1).

Further information on the transformations that occur in the glass would be provided by *in situ* diffraction experiments that access a large scattering vector range, thereby improving the resolution in real space. Issues to be addressed include the relation between glass structure and network rigidity with increasing pressure [101, 102]. Additional information on densification mechanisms would be provided by using *ab initio* methods and some exploratory work, to study the structural, vibrational and electronic properties of the GeS_2 system at ambient pressure, has been made [93, 103–108]. Indeed, since the present manuscript was submitted, *ab initio* molecular dynamics methods have now been applied to study several of the properties of GeS_2 at pressures up to 60 GPa [109]. A detailed account of this material in the pressure–temperature regime studied in the present work was not, however, given.

Acknowledgments

We thank Richard Martin (Bath) for preparing the GeS_2 sample used for the ID30 experiment and Duncan Francis (ISIS Facility) for providing us with Ti–Zr gaskets. For the ILL experiments we thank Pierre Palleau, Alain Bertoni, Jean-Luc Laborier and Claude Payre. We also thank the EPSRC for financial support and for providing its Chemical Database Service. It is a pleasure to acknowledge the support that Richard Palmer has given over many years to research on liquid and amorphous materials.

Appendix A. The Fourier transformation of x-ray total structure factors and the extraction of coordination numbers

The expression that relates a partial structure factor $S_{\alpha\beta}(k)$ to the partial pair distribution function $g_{\alpha\beta}(r)$ for an isotropic

system is the sine Fourier transform

$$g_{\alpha\beta}(r) - 1 = \frac{1}{2\pi^2 n_0 r}\int_0^\infty \mathrm{d}k\, k[S_{\alpha\beta}(k) - 1]\sin(kr) \quad \text{(A.1)}$$

where n_0 is the atomic number density. This equation can be re-written as the Fourier transform

$$-2\pi\, \mathrm{i}n_0\, r[g_{\alpha\beta}(r) - 1] = \frac{1}{2\pi}\int_{-\infty}^\infty \mathrm{d}k\, k[S_{\alpha\beta}(k) - 1]\exp(-\mathrm{i}kr) \quad \text{(A.2)}$$

where $S_{\alpha\beta}(k)$ has been extended to negative argument by defining it as an even function and $\mathrm{i} = \sqrt{-1}$. If a modification function $M(k)$ is included, the x-ray total structure factor given by equation (3) can be re-defined as

$$S'_{\mathrm{X}}(k) - 1 \equiv \frac{F(k)M(k)}{|\langle f(k)\rangle|^2} = \sum_{\alpha=1}^n\sum_{\beta=1}^n \mathcal{M}_{\alpha\beta}(k)[S_{\alpha\beta}(k) - 1] \quad \text{(A.3)}$$

where the weighting factors for each $S_{\alpha\beta}(k)$ function are given by

$$\mathcal{M}_{\alpha\beta}(k) = \frac{c_\alpha c_\beta f_\alpha(k) f^*_\beta(k)}{|\langle f(k)\rangle|^2} M(k) \quad \text{(A.4)}$$

and $M(k)$ is defined so that $M(k = 0) = 1$. The Fourier transform of the even function $\mathcal{M}_{\alpha\beta}(k)$ is given by

$$\widetilde{\mathcal{M}}_{\alpha\beta}(r) = \frac{1}{2\pi}\int_{-\infty}^\infty \mathrm{d}k\, \mathcal{M}_{\alpha\beta}(k)\exp(-\mathrm{i}kr). \quad \text{(A.5)}$$

By the one-dimensional convolution theorem [110] it follows that, after the inclusion of $\mathcal{M}_{\alpha\beta}(k)$, equation (A.2) can be re-written as

$$\begin{aligned}
&-2\pi\mathrm{i}n_0\, r h_{\alpha\beta}(r) \\
&\equiv \frac{1}{2\pi}\int_{-\infty}^\infty \mathrm{d}k\, k[S_{\alpha\beta}(k) - 1]\mathcal{M}_{\alpha\beta}(k)\exp(-\mathrm{i}kr) \\
&= -2\pi\mathrm{i}n_0\, r[g_{\alpha\beta}(r) - 1] \otimes \widetilde{\mathcal{M}}_{\alpha\beta}(r) \quad \text{(A.6)}
\end{aligned}$$

where $\otimes$ denotes the one-dimensional convolution operator. If we consider the partial pair distribution function

$$d_{\alpha\beta}(r) = 4\pi\, n_0\, r[g_{\alpha\beta}(r) - 1] \quad \text{(A.7)}$$

and we define

$$d'_{\alpha\beta}(r) \equiv 4\pi\, n_0\, r h_{\alpha\beta}(r) \quad \text{(A.8)}$$

then equation (A.6) can be re-written as

$$\begin{aligned}
&d'_{\alpha\beta}(r) \\
&= d_{\alpha\beta}(r) \otimes \widetilde{\mathcal{M}}_{\alpha\beta}(r) \\
&= 4\pi\, n_0 \int_{-\infty}^\infty \mathrm{d}r'\, r' g_{\alpha\beta}(r')\widetilde{\mathcal{M}}_{\alpha\beta}(r - r') \\
&\quad - 4\pi\, n_0 \int_{-\infty}^\infty \mathrm{d}r'\, r'\widetilde{\mathcal{M}}_{\alpha\beta}(r - r') \\
&= 4\pi\, n_0 \int_{-\infty}^\infty \mathrm{d}r'\, r' g_{\alpha\beta}(r')\widetilde{\mathcal{M}}_{\alpha\beta}(r - r') \\
&\quad - 4\pi\, n_0\, r\mathcal{M}_{\alpha\beta}(k = 0) \quad \text{(A.9)}
\end{aligned}$$

where we have used the expression for the inverse Fourier transform of equation (A.5)

$$\mathcal{M}_{\alpha\beta}(k) = \int_{-\infty}^\infty \mathrm{d}r\, \widetilde{\mathcal{M}}_{\alpha\beta}(r)\exp(\mathrm{i}kr) \quad \text{(A.10)}$$

which gives $\int_{-\infty}^\infty \mathrm{d}r\, \widetilde{\mathcal{M}}_{\alpha\beta}(r) = \mathcal{M}_{\alpha\beta}\ (k = 0)$. The r space representation of the x-ray total structure factor of equation (A.3) is given by the total pair distribution function $G'(r)$ which is defined by equation (6). This expression can be re-written as the Fourier transform

$$\begin{aligned}
&-2\pi\, \mathrm{i}n_0\, r[G'_{\mathrm{X}}(r) - 1] \\
&= \frac{1}{2\pi}\int_{-\infty}^\infty \mathrm{d}k\, k[S_{\mathrm{X}}(k) - 1]M(k)\exp(-\mathrm{i}kr) \\
&= -2\pi\mathrm{i}n_0\, r\sum_{\alpha=1}^n\sum_{\beta=1}^n h_{\alpha\beta}(r) \quad \text{(A.11)}
\end{aligned}$$

where the last line follows from equation (A.6). Hence, by using equation (A.8), the total pair correlation function $D'_{\mathrm{X}}(r)$ can be defined where

$$D'_{\mathrm{X}}(r) = 4\pi\, n_0\, r[G'_{\mathrm{X}}(r) - 1] = \sum_{\alpha=1}^n\sum_{\beta=1}^n d'_{\alpha\beta}(r). \quad \text{(A.12)}$$

At r values smaller than the distance of closest approach between the centre of two atoms where $g_{\alpha\beta}(r) = g_{\alpha\beta}(r = 0) = 0$ it follows that

$$D'_{\mathrm{X}}(r) = -4\pi\, n_0\, r\sum_{\alpha=1}^n\sum_{\beta=1}^n \mathcal{M}_{\alpha\beta}(k = 0) = -4\pi\, n_0\, r \quad \text{(A.13)}$$

since $M(k = 0) = 1$. Then the limiting value of $G'_{\mathrm{X}}(r) = G'_{\mathrm{X}}(r = 0) = 0$.

If there is a clearly defined peak in $G'_{\mathrm{X}}(r)$ that can be attributed to a specific partial pair distribution function $g_{\alpha\beta}(r)$ then the coordination number $\bar{n}^\beta_\alpha$ of chemical species β around α can be obtained by direct integration over that peak once a suitably weighted k space function has been Fourier transformed. For instance, if a peak can be attributed solely to $g_{11}(r)$ then it is convenient to define a modified x-ray total structure factor

$$\begin{aligned}
{}^{\mathrm{mod}}S'_{\mathrm{X}}(k) - 1 &\equiv \frac{F(k)M(k)}{c_1^2|f_1(k)|^2} \\
&= \sum_{\alpha=1}^n\sum_{\beta=1}^n {}^{\mathrm{mod}}\mathcal{M}_{\alpha\beta}(k)[S_{\alpha\beta}(k) - 1] \quad \text{(A.14)}
\end{aligned}$$

where

$${}^{\mathrm{mod}}\mathcal{M}_{\alpha\beta}(k) = \frac{c_\alpha c_\beta f_\alpha(k) f^*_\beta(k)}{c_1^2|f_1(k)|^2} M(k) \quad \text{(A.15)}$$

so that the weighting factor for the $[S_{11}(k) - 1]$ term is simply $M(k)$. The r space representation of the modified x-ray total structure factor defined by equation (A.15) is given by

$${}^{\mathrm{mod}}D'_{\mathrm{X}}(r) = 4\pi\, n_0\, r[{}^{\mathrm{mod}}G'_{\mathrm{X}}(r) - 1] = \sum_{\alpha=1}^n\sum_{\beta=1}^n {}^{\mathrm{mod}}d'_{\alpha\beta}(r) \quad \text{(A.16)}$$

where the ${}^{\mathrm{mod}}d'_{\alpha\beta}(r)$ functions are defined by equation (A.9) after $\widetilde{\mathcal{M}}_{\alpha\beta}(r)$ and $\mathcal{M}_{\alpha\beta}(k = 0)$ are replaced by ${}^{\mathrm{mod}}\widetilde{\mathcal{M}}_{\alpha\beta}(r)$ and ${}^{\mathrm{mod}}\mathcal{M}_{\alpha\beta}(k = 0)$, respectively. For r values smaller than the

distance of closest approach between the centre of two atoms

$$^{\mathrm{mod}}D'_{\mathrm{X}}(r) = -4\pi\, n_0\, r \sum_{\alpha=1}^{n}\sum_{\beta=1}^{n} {}^{\mathrm{mod}}\mathcal{M}_{\alpha\beta}(k=0)$$
$$= -4\pi\, n_0\, r\left\{1 + \underbrace{\sum_{\alpha=1}^{n}\sum_{\beta=1}^{n}}_{\beta\neq 1 \mathrm{if} \alpha=1} {}^{\mathrm{mod}}\mathcal{M}_{\alpha\beta}(k=0)\right\} \quad \text{(A.17)}$$

since $M(k=0)=1$. Then the small r limiting value of $^{\mathrm{mod}}G'_{\mathrm{X}}(r)$ is given by $^{\mathrm{mod}}G'_{\mathrm{X}}(r=0) = 1 + {}^{\mathrm{mod}}D'_{\mathrm{X}}(r)/4\pi n_0 r$ where $^{\mathrm{mod}}D'_{\mathrm{X}}(r)$ is given by equation (A.17) such that $^{\mathrm{mod}}G'_{\mathrm{X}}(r=0)$ takes a finite value. Thus, if r_i and r_j define the starting and finishing r values of a well defined peak in $^{\mathrm{mod}}G'_{\mathrm{X}}(r)$ that can be attributed solely to $g_{11}(r)$ then the corresponding coordination number defined by equation (5) is given by

$$\bar{n}_1^1 = 4\pi\, n_0\, c_1 \int_{r_i}^{r_j} \mathrm{d}r\, r^2[{}^{\mathrm{mod}}G'_{\mathrm{X}}(r) - {}^{\mathrm{mod}}G'_{\mathrm{X}}(r=0)] \quad \text{(A.18)}$$

since $g_{11}(r) = [{}^{\mathrm{mod}}G'_{\mathrm{X}}(r) - {}^{\mathrm{mod}}G'_{\mathrm{X}}(r=0)]$ for the range $r_i \leqslant r \leqslant r_j$.

For example, in the case of glassy GeS_2 for which $c_{\mathrm{Ge}} = 1/3$, $c_{\mathrm{S}} = 2/3$ and, in electron units, $f_{\mathrm{Ge}}(k=0) = 32$, $f_{\mathrm{S}}(k=0) = 16$ the Ge–Ge coordination number, $\bar{n}_{\mathrm{Ge}}^{\mathrm{Ge}}$, for the peak corresponding to edge-sharing tetrahedra can be readily found by using equation (A.18) wherein $^{\mathrm{mod}}G'_{\mathrm{X}}(r=0) = -3$. Alternatively, to obtain the nearest-neighbour Ge–S coordination number, $\bar{n}_{\mathrm{Ge}}^{\mathrm{S}}$, the modified x-ray total structure factor of equation (A.14) needs to be re-defined as $^{\mathrm{mod}}S'_{\mathrm{X}}(k) - 1 \equiv F(k)M(k)/\{c_1c_2[f_1^*(k)f_2(k) + f_1(k)f_2^*(k)]\}$ and, by using the same arguments outlined above, it follows that if the first peak in the new $^{\mathrm{mod}}G'_{\mathrm{X}}(r)$ function can be attributed solely to $g_{\mathrm{GeS}}(r)$ where r_i and r_j define its boundaries then $\bar{n}_{\mathrm{Ge}}^{\mathrm{S}} = 4\pi\, n_0\, c_{\mathrm{S}} \int_{r_i}^{r_j} \mathrm{d}r\, r^2[{}^{\mathrm{mod}}G'_{\mathrm{X}}(r) - {}^{\mathrm{mod}}G'_{\mathrm{X}}(r=0)]$ where $^{\mathrm{mod}}G'_{\mathrm{X}}(r=0) = -1$.

Appendix B. The lozenge correction

An oscillating radial collimator system, as used in the x-ray diffractometer set-up of the present work, allows for a considerable reduction in the scattered intensity that is observed from a sample container and gasket in high pressure experiments [56]. This is illustrated in figure B.1 which shows the observed scattering volume at different scattering angles 2θ assuming that the incident beam is perfectly parallel collimated and the detector system defines a scattered beam with similar perfect collimation and the *same* width w. The sample, its boron nitride (BN) container and the gasket are all assumed to have cylindrical geometry while the incident and scattered beams are both in a plane perpendicular to the axis of symmetry and have an equal height h. In the following we will assume, for simplicity of notation, that h takes a value of unity.

By inspection of figure B.1(a) it can be seen that at large scattering angles the observed scattering volume is situated totally in the sample such that there will be no contribution to the measured signal from either the container or gasket. As the scattering angle is decreased, a critical angle ψ_{c} is reached (figure B.1(b)) below which the observed scattering volume will include a portion of the container (figure B.1(c)). As the scattering angle is reduced further, a second critical angle ϕ_{c} is reached below which the observed scattering volume will also have a contribution from the gasket (figure B.1(d)). Thus, in order to obtain a normalized differential scattering cross-section due solely to the sample, the appropriate amount of scattering from the container and gasket needs to be subtracted from the observed signal at each 2θ value and the change in scattering volume of the sample with 2θ also needs to be taken into account. In principle, it is also necessary to correct for the self-attenuation of the incident and scattered beams by the sample, container and gasket materials, the effect of which will depend on the nature of the materials and the x-ray energy [111]. However, for the x-ray energies used in the present experiment, Monte Carlo simulations of the attenuation corrections show they are small compared to other experimental errors (such as changes in geometry due to distortions of the pressure cell) and they were therefore not included in our analysis procedure. The corrections we have applied in practice are described below.

Appendix B.1. Calculation of the critical angles ψ_{c} and ϕ_{c}

Consider the case when the incident and scattered beams have the same width w. Then figure B.2 shows the point at which the observed scattering volume from the sample reaches the inner container wall as the scattering angle 2θ is decreased. By geometry it can be seen that this critical angle is given by

$$\psi_{\mathrm{c}} = 2\arcsin\left(\frac{w}{2r_{\mathrm{s}}}\right) \quad \text{(B.1)}$$

where r_{s} is the radius of the sample cylinder. Using the same geometry, we also obtain the result that the observed scattering volume will include a contribution from the gasket below the critical angle

$$\phi_{\mathrm{c}} = 2\arcsin\left(\frac{w}{2\,r_{\mathrm{BN}}}\right) \quad \text{(B.2)}$$

where r_{BN} is the outer radius of the boron nitride container. Hence for $2\theta > \psi_{\mathrm{c}}$ scattering is only observed from the sample, for $\phi_{\mathrm{c}} < 2\theta < \psi_{\mathrm{c}}$ scattering is observed from the sample and container, and for $2\theta < \phi_{\mathrm{c}}$ scattering is observed from the sample, container and gasket. There is also an angle, χ_{c}, for which the observed scattering volume reaches the outer gasket wall. In our experiments this takes a very small value and its effect would correspond to a reduction in our already small gasket scattering at low angles. We have therefore not applied this correction.

Appendix B.2. Calculation of the sample, container and gasket scattering volumes

Appendix B.2.1. $2\theta > \psi_{\mathrm{c}}$. At these angles the observed scattering comes only from the lozenge shaped area in the centre of the sample (see figure B.2). In this case the scattering volume of the sample is found by using the area of a parallelepiped and may be expressed as

$$V_{\mathrm{s}} = \frac{w^2}{\sin(2\theta)}. \quad \text{(B.3)}$$

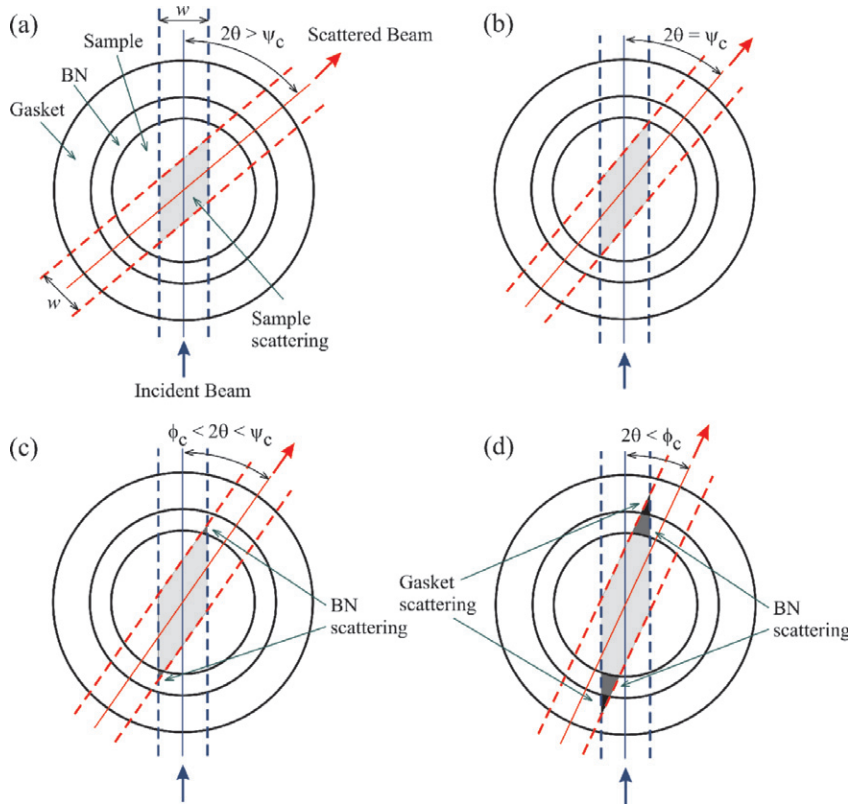

Figure B.1. Representation of the observed scattering volumes at different scattering angles 2θ. (a) At large scattering angles the scattering volume is located solely in the sample region (light grey shaded region). (b) When the scattering angle is decreased below the critical value ψ_c the scattering volume will start to include parts of the boron nitride (BN) container. (c) For $\phi_c < 2\theta < \psi_c$ the scattering volume includes parts of the sample (light grey shaded region) and the BN container (dark grey shaded region). (d) For $2\theta < \phi_c$ the scattering volume includes parts of the sample (light grey shaded region), BN container (dark grey shaded region) and gasket (solid black shaded region).

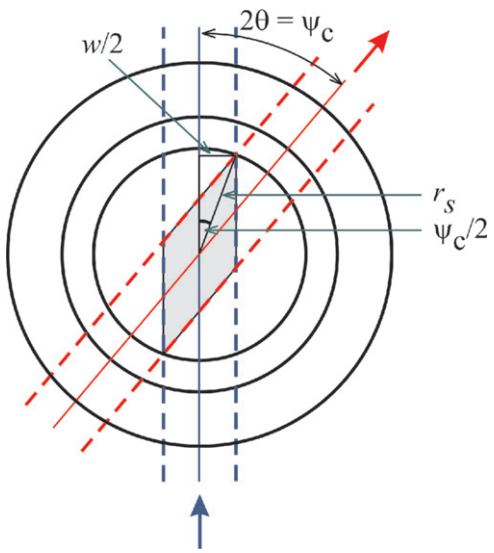

Figure B.2. The geometry for evaluating the critical scattering angle ψ_c of equation (B.1). For scattering angles $2\theta < \psi_c$ scattering from the BN container is seen by the detector.

Appendix B.2.2. $\phi_c < 2\theta < \psi_c$. Between these angles there are contributions to the observed scattering from both the sample and two small sections of the boron nitride container (see figure B.3). The observed scattering volume of the sample may be calculated from the areas of the sections marked *a, b* and *c* in figure B.3(a). The four sections of shape *a* correspond to half of the total area of the lozenge defined by the incoming beam and detector collimation giving a volume

$$V_a = \frac{1}{2}\frac{w^2}{\sin(2\theta)}. \tag{B.4}$$

The four sections of shape *b* are of identical volume by symmetry and may be determined by reference to the angle α marked in figure B.3(b) where

$$\alpha = 2\theta - \frac{\psi_c}{2} \tag{B.5}$$

and ψ_c is the critical angle given by equation (B.1). Hence the total volume of the four triangular sections marked as *b* may be written as

$$V_b = 4 \times \frac{1}{2}\frac{w}{2\sin(2\theta)} r_s \sin\alpha = \frac{w r_s}{\sin(2\theta)} \sin\alpha. \tag{B.6}$$

Finally, the volume of the two identical sections of shape *c* is determined from the area of a circular segment with angle $2(\theta - \alpha)$ and is hence equal to

$$V_c = 2(\theta - \alpha) r_s^2. \tag{B.7}$$

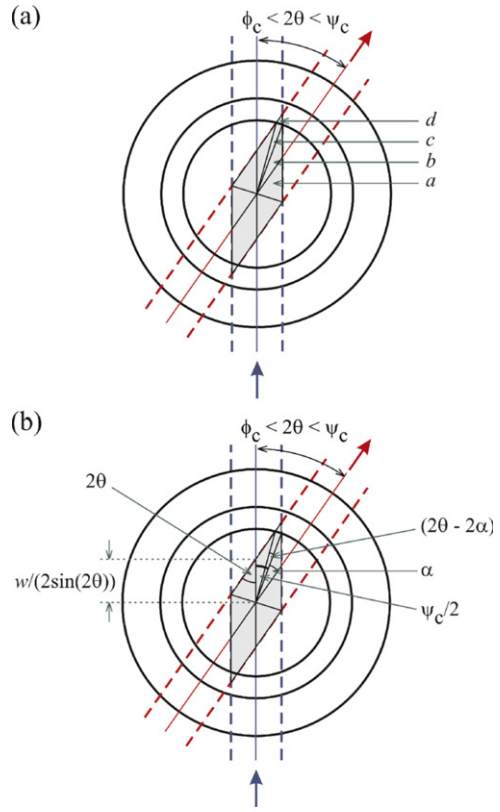

Figure B.3. Details of the sections used to calculate the observed scattering volumes for the sample and BN container when $\phi_c < 2\theta < \psi_c$. In (a) the sections of type a, b and c that lie within the sample and the section of type d that lies within the container are identified. In (b) several of the angles and length $w/2\sin(2\theta)$ used in the derivation of equations (B.4)–(B.9) are identified.

Thus the total volume of the sample that contributes to the observed scattering is

$$V_s = V_a + V_b + V_c = \frac{1}{2}\frac{w^2}{\sin(2\theta)} + \frac{wr_s}{\sin(2\theta)}\sin\alpha + 2(\theta-\alpha)r_s^2. \tag{B.8}$$

The volume of the boron nitride container that contributes to the scattering is indicated by the two triangular-like sections marked as d in figure B.3(a). This volume can be simply calculated as the volume of the large lozenge (again given by equation (B.3)) minus the scattering volume of the sample calculated above i.e.

$$V_{BN} = \frac{w^2}{\sin(2\theta)} - V_s. \tag{B.9}$$

Appendix B.2.3. $2\theta < \phi_c$. As the scattering angle decreases below ϕ_c scattered intensity will be observed from the epoxy gasket of the pressure cell. In this region the observed sample scattering volume is still given by equation (B.8). However, the observed scattering volume of the boron nitride container is no longer given by equation (B.9) due to the two small triangular-like sections of the lozenge with volume V_g that cut into the gasket. By using the same arguments outlined in appendix B.2.2 this volume may be written as

$$V_g = \frac{w^2}{\sin(2\theta)} - \left\{\frac{1}{2}\frac{w^2}{\sin(2\theta)} + \frac{wr_s}{\sin(2\theta)}\sin\beta + 2(\theta-\beta)r_s^2\right\} \tag{B.10}$$

where β is defined as

$$\beta = 2\theta - \frac{\phi_c}{2}. \tag{B.11}$$

The observed scattering volume of the boron nitride container is

$$V'_{BN} = V_{BN} - V_g \tag{B.12}$$

where V_{BN} is given by equation (B.9).

We note that if the height h of both the incident and scattered beams is not equal to unity then all of the above expressions for the volume will need to be multiplied by the beam height.

Appendix B.3. Application of the corrections

In principle, in the limit when the self-attenuation corrections are negligible, the container/gasket subtraction could be made by measuring the scattering with and without the sample in the container/gasket assembly and simply subtracting the container/gasket scattering to leave only the scattering due to the sample. At this point equation (B.8) would be sufficient to correct the data for the 2θ dependent change in the observed sample scattering volume. Although this procedure may be carried out under ambient conditions, it is impractical after the system has been pressurized since the density of the various materials will generally have a different pressure dependence, some distortion of the pressure cell may take place (changing its effective dimensions), the Bragg scattering from the container will change as its material is compressed, and there will be a radial pressure gradient with most of the gasket at a lower compression than the sample. We therefore adopted the following strategy.

At each pressure the cell was moved sideways relative to the incident beam so that the centre of scattering was located firstly in the container annulus and then in the gasket annulus. This enabled us to obtain diffraction patterns dominated by either the container or the gasket scattering and, for each 2θ angle, the truncated lozenge shaped scattering volume of the container or gasket was calculated. The scattering per unit volume for both the container and gasket materials was thereby obtained as a function of 2θ. To provide an *estimate* of the container and gasket scattering when the cell is positioned so that the incident beam passes directly through the sample centre, the results were multiplied by either the container volume calculated in equation (B.9) ($= 0$ for $2\theta > \psi_c$) or the gasket volume calculated in equation (B.10) ($= 0$ for $2\theta > \phi_c$). At this point, the scattering from the sample was obtained by subtracting these weighted contributions from the diffraction pattern measured for the sample centred in the incident beam and the data were finally normalized according to equation (B.8). In practice, it was also necessary to refine the value used for the sample radius in the calculations in order to compensate for changes in the cell dimensions with change of pressure.

Appendix B.4. Generalization to other container configurations and beam geometries

For diffraction experiments made at high pressures *and* high temperatures, a cylindrical graphite heater is placed between the BN sample container and gasket. This will lead to another critical angle $2\theta = \nu_c$ just above which the observed scattering volume will have a contribution from the sample and BN container and just below which the observed scattering volume will have a contribution from the sample, BN container and graphite heater. The formalism of this appendix can be readily generalized to account for this change of container configuration.

The formalism of this appendix can also be adapted to account for changes in the beam geometry and the results obtained above will provide a benchmark for assessing the effect of these changes. For example, a scattered parallel beam need not have the same width as the incident beam and the observed scattering volume sketched in figure B.1 is then calculated by considering the area of a parallelogram with opposite pairs of sides having unequal length. Additionally, the collimation system will generally define a non-parallel scattered beam, leading to an observed scattering volume with a trapezoidal cross-section, and there will also be issues associated with the beam umbra/penumbra. Also, although the sample in the x-ray beam is aligned to maximize the measured intensity, this position may not correspond to the axis of the sample being placed exactly at the geometrical centre of the diffractometer owing to attenuation of the incident and scattered beams and sample distortion effects. In practice, given the other experimental uncertainties, the equations derived in this appendix can still be used as an effective guide for estimating the various contributions to the observed scattering (the 2θ dependence of the observed sample scattering volume is particularly important in this context), especially if the variation in beam geometry is small.

References

[1] Boolchand P (ed) 2000 *Insulating and Semiconducting Glasses* (Singapore: World Scientific)
[2] Salmon P S, Martin R A, Mason P E and Cuello G J 2005 *Nature* **435** 75
[3] Salmon P S 2005 *J. Phys.: Condens. Matter* **17** S3537
[4] Salmon P S, Barnes A C, Martin R A and Cuello G J 2006 *Phys. Rev. Lett.* **96** 235502
[5] Salmon P S 2006 *J. Phys.: Condens. Matter* **18** 11443
[6] Salmon P S 2007 *J. Phys.: Condens. Matter* **19** 455208
[7] Moss S C and Price D L 1985 *Physics of Disordered Materials* ed D Adler, H Fritzsche and S R Ovshinsky (New York: Plenum) p 77
[8] Elliott S R 1991 *Nature* **354** 445
[9] Salmon P S 1994 *Proc. R. Soc.* A **445** 351
[10] Angell C A 1995 *Science* **267** 1924
[11] Salmon P S, Barnes A C, Martin R A and Cuello G J 2007 *J. Phys.: Condens. Matter* **19** 415110
[12] Guthrie M, Tulk C A, Benmore C J, Xu J, Yarger J L, Klug D D, Tse J S, Mao H-K and Hemley R J 2004 *Phys. Rev. Lett.* **93** 115502
[13] Stølen S, Grande T and Johnsen H-B 2002 *Phys. Chem. Chem. Phys.* **4** 3396
[14] Petri I, Salmon P S and Fischer H E 2000 *Phys. Rev. Lett.* **84** 2413
[15] Salmon P S and Petri I 2003 *J. Phys.: Condens. Matter* **15** S1509
[16] Mei Q, Benmore C J, Hart R T, Bychkov E, Salmon P S, Martin C D, Michel F M, Antao S M, Chupas P J, Lee P L, Shastri S D, Parise J B, Leinenweber K, Amin S and Yarger J L 2006 *Phys. Rev.* B **74** 014203
[17] Crichton W A, Mezouar M, Grande T, Stølen S and Grzechnik A 2001 *Nature* **414** 622
[18] Ruska J and Thurn H 1976 *J. Non-Cryst. Solids* **22** 277
[19] Penfold I T and Salmon P S 1991 *Phys. Rev. Lett.* **67** 97
[20] Petri I, Salmon P S and Howells W S 1999 *J. Phys.: Condens. Matter* **11** 10219
[21] Weinstein B A, Zallen R, Slade M L and Mikkelsen J C Jr 1982 *Phys. Rev.* B **25** 781
[22] Dittmar G and Schäfer H 1975 *Acta Crystallogr.* B **31** 2060
[23] Dittmar G and Schäfer H 1976 *Acta Crystallogr.* B **32** 1188
[24] Poole P H, Grande T, Angell C A and McMillan P F 1997 *Science* **275** 322
[25] Dittmar G and Schäfer H 1976 *Acta Crystallogr.* B **32** 2726
[26] Feltz A, Pohle M, Steil H and Herms G 1985 *J. Non-Cryst. Solids* **69** 271
[27] Armand P, Ibanez A, Philippot E, Ma Q and Raoux D 1992 *J. Non-Cryst. Solids* **150** 371
[28] Nagata Y, Kokai S, Uemura O and Kameda Y 1994 *J. Non-Cryst. Solids* **169** 104
[29] Petri I and Salmon P S 2001 *J. Non-Cryst. Solids* **293–295** 169
[30] Salmon P S 2007 *J. Non-Cryst. Solids* **353** 2959
[31] Bhatia A B and Thornton D E 1970 *Phys. Rev.* B **2** 3004
[32] Salmon P S 1992 *Proc. R. Soc.* A **437** 591
[33] Salmon P S and Liu J 1994 *J. Phys.: Condens. Matter* **6** 1449
[34] Shimada M and Dachille F 1977 *Inorg. Chem.* **16** 2094
[35] Miyauchi K, Qiu J, Shojiya M, Kawamoto Y and Kitamura N 2001 *J. Non-Cryst. Solids* **279** 186
[36] Tanaka K 1987 *J. Non-Cryst. Solids* **90** 363
[37] Málek J and Shánělová J 1999 *J. Non-Cryst. Solids* **243** 116
[38] Nemilov S V 2007 *J. Non-Cryst. Solids* **353** 4613
[39] Fischer H E, Barnes A C and Salmon P S 2006 *Rep. Prog. Phys.* **69** 233
[40] Faber T E and Ziman J M 1965 *Phil. Mag.* **11** 153
[41] Lorch E 1969 *J. Phys. C: Solid State Phys.* **2** 229
[42] Sears V F 1992 *Neutron News* **3** 26
[43] Penfold I T and Salmon P S 1989 *J. Non-Cryst. Solids* **114** 82
[44] Boolchand P, Grothaus J, Tenhover M, Hazle M A and Grasselli R K 1986 *Phys. Rev.* B **33** 5421
[45] Málek J 1989 *J. Non-Cryst. Solids* **107** 323
[46] Kawamoto Y and Tsuchihashi S 1971 *J. Am. Ceram. Soc.* **54** 526
[47] Feng X, Bresser W J and Boolchand P 1997 *Phys. Rev. Lett.* **78** 4422
[48] Cai L and Boolchand P 2002 *Phil. Mag.* B **82** 1649
[49] Hannon A C 2005 *Nucl. Instrum. Methods Phys. Res.* A **551** 88
[50] www.isis.rl.ac.uk/disordered/Manuals/gudrun/Gudrun_manual_2006.pdf
[51] Jal J F, Mathieu C, Chieux P and Dupuy J 1990 *Phil. Mag.* B **62** 351
[52] Salmon P S, Xin S and Fischer H E 1998 *Phys. Rev.* B **58** 6115
[53] Urquidi J, Benmore C J, Neuefeind J and Tomberli B 2003 *J. Appl. Crystallogr* **36** 368
[54] Maslen E N, Fox A G and O'Keefe M A 1995 *International Tables for Crystallography* vol C, ed A J C Wilson (Dordrecht: Kluwer) section 6.1.1, p 476
[55] Cromer D T 1969 *J. Chem. Phys.* **50** 4857
[56] Mezouar M, Faure P, Crichton W A, Rambert N, Sitaud B, Bauchau S and Blattmann G 2002 *Rev. Sci. Instrum.* **73** 3570
[57] Le Godec Y, Martinez-Garcia D, Mezouar M, Syfosse G, Itie J P and Besson J-M 2000 *Science and Technology of*

High Pressure vol 2, ed M H Manghnani, W J Nellis and M F Nicol (Hyderabad, India: Universities Press) p 925
[58] Heinz D L and Jeanloz R 1984 *J. Appl. Phys.* **55** 885
[59] Anderson O L, Isaak D G and Yamamoto S 1989 *J. Appl. Phys.* **65** 1534
[60] Hammersley A P, Internal Report No. ESRF98HA01T, European Synchrotron Radiation Facility, Grenoble, France, 1998 (unpublished)
[61] Hubbell J H, Veigele Wm J, Briggs E A, Brown R T, Cromer D T and Howerton R J 1975 *J. Phys. Chem. Ref. Data* **4** 471
[62] Bull C L, Guthrie M, Klotz S, Philippe J, Strässle Th, Nelmes R J, Loveday J S and Hamel G 2005 *High Pressure Res.* **25** 229
[63] Klotz S, Strässle Th, Rousse G, Hamel G and Pomjakushin V 2005 *Appl. Phys. Lett.* **86** 031917
[64] Fischer H E, Cuello G J, Palleau P, Feltin D, Barnes A C, Badyal Y S and Simonson J M 2002 *Appl. Phys.* A **74** S160
[65] Klotz S, Padmanabhan B, Philippe J and Strässle Th 2008 *High Pressure Research* **28** 621
[66] Bertagnolli H, Chieux P and Zeidler M D 1976 *Mol. Phys.* **32** 759
[67] Drewitt J W E, Salmon P S, Barnes A C, Klotz S, Fischer H E and Crichton W A 2009 submitted
[68] Penfold I T and Salmon P S 1990 *J. Phys.: Condens. Matter* **2** SA233
[69] Zachariasen W H 1936 *J. Chem. Phys.* **4** 618
[70] Prewitt C T and Young H S 1965 *Science* **149** 535
[71] MacLachlan M J, Petrov S, Bedard R L, Manners I and Ozin G A 1998 *Angew. Chem. Int. Edn* **37** 2075
[72] Onari S, Inokuma T, Kataura H and Arai T 1987 *Phys. Rev.* B **35** 4373
[73] Kawamoto Y, Miyauchi K, Shojiya M, Sakida S and Kitamura N 2001 *J. Non-Cryst. Solids* **284** 128
[74] Maruyama K, Ebata H, Suzuki S, Misawa M, Takeda S and Kawakita Y 1999 *J. Non-Cryst. Solids* **250–252** 483
[75] Shirley R 2002 *The Crysfire 2002 System for Automatic Powder Indexing: User's Manual* (Surrey, UK: The Lattice Press)
[76] Visser J W 1969 *J. Appl. Crystallogr.* **2** 89
[77] Werner P-E, Eriksson L and Westdahl M 1985 *J. Appl. Crystallogr.* **18** 367
[78] Taupin D 1968 *J. Appl. Crystallogr.* **1** 178
[79] Laugier J and Bochu B 2004 http://www.lmgp.inpg.fr/, available from http://www.ccp14.ac.uk/
[80] Le Bail A, Duroy H and Fourquet J L 1988 *Mater. Res. Bull.* **23** 447
[81] Larson A C and Von Dreele R B 1994 General structure analysis system (GSAS) *Los Alamos National Laboratory* Report LAUR 86-748
[82] Grande T, Ishii M, Akaishi M, Aasland S, Fjellvåg H and Stølen S 1999 *J. Solid State Chem.* **145** 167
[83] Brehler B 1959 *Naturwissenschaften* **46** 554
[84] Oswald H R and Jaggi H 1960 *Helv. Chim. Acta* **43** 72
[85] Brehler B 1961 *Zeitschrift für Kristallographie, Kristallgeometrie, Kristallphysik, Kristallchemie* **115** 373
[86] Grzechnik A, Stølen S, Bakken E, Grande T and Mezouar M 2000 *J. Solid State Chem.* **150** 121
[87] Hahn T (ed) 1996 *International Tables for Crystallography* vol A (Dordrecht: Kluwer)
[88] Lin C, Busse L E, Nagel S R and Faber J 1984 *Phys. Rev.* B **29** 5060
[89] Drahokoupil J, Smotlacha O, Fendrych F and Klokočníková H 1986 *J. Non-Cryst. Solids* **88** 43
[90] Armand P, Ibanez A, Dexpert H and Philippot E 1992 *J. Non-Cryst. Solids* **139** 137
[91] Bychkov E, Miloshova M, Price D L, Benmore C J and Lorriaux A 2006 *J. Non-Cryst. Solids* **352** 63
[92] Kotsalas I P and Raptis C 2001 *Phys. Rev.* B **64** 125210
[93] Holomb R, Johansson P, Mitsa V and Rosola I 2005 *Phil. Mag.* **85** 2947
[94] Miyauchi K, Qiu J, Shojiya M, Kawamoto Y, Kitamura N, Fukumi K, Katayama Y and Nishihata Y 2002 *Solid State Commun.* **124** 189
[95] Perakis A, Kotsalas I P, Pavlatou E A and Raptis C 1999 *Phys. Status Solidi* b **211** 421
[96] Kotsalas I P and Raptis C 2001 *J. Optoelectron. Adv. Mater.* **3** 675
[97] Weinstein B A and Slade M L 1984 Optical effects in amorphous semiconductors *American Institute of Physics Conference Proceedings Number 120* ed P C Taylor and S G Bishop (New York: American Institute of Physics)
[98] Popović Z V, Holtz M, Reimann K and Syassen K 1996 *Phys. Status Solidi* b **198** 533
[99] Antao S M, Benmore C J, Li B, Wang L, Bychkov E and Parise J B 2008 *Phys. Rev. Lett.* **100** 115501
[100] Wang F, Mamedov S, Boolchand P, Goodman B and Chandrasekhar M 2005 *Phys. Rev.* B **71** 174201
[101] Trachenko K and Dove M T 2003 *Phys. Rev.* B **67** 212203
[102] Trachenko K, Dove M T, Brazhkin V V and El'kin F S 2004 *Phys. Rev. Lett.* **93** 135502
[103] Jackson K, Briley A, Grossman S, Porezag D V and Pederson M R 1999 *Phys. Rev.* B **60** R14985
[104] Hachiya K 2002 *J. Non-Cryst. Solids* **312–314** 566
[105] Blaineau S, Jund P and Drabold D A 2003 *Phys. Rev.* B **67** 094204
[106] Blaineau S and Jund P 2004 *Phys. Rev.* B **69** 064201
[107] Blaineau S, Le Roux S and Jund P 2007 *J. Phys.: Condens. Matter* **19** 455207
[108] Le Roux S and Jund P 2007 *J. Phys.: Condens. Matter* **19** 196102
[109] Durandurdu M 2009 *Phys. Rev.* B **79** 205202
[110] Champeney D C 1973 *Fourier Transforms and their Physical Applications* (London: Academic Press)
[111] Paalman H H and Pings C J 1962 *J. Appl. Phys.* **33** 2635